Scuola Dottorale EDEMOM

European Doctorate in Electronic Materials,
Optoelectronics and Microsystems

XXIV ciclo

Ph.D. Thesis

Optical Characterization of Lithium Fluoride X-ray Imaging Detectors

Schirin Heidari Bateni

Tutors:
Prof. Fabrizia Somma
Dr. Rosa Maria Montereali
Coordinator:
Prof. Giuseppe Schirripa Spagnolo

February 2012

Scuola Dottorale EDEMOM

European Doctorate in Electronic Materials,
Optoelectronics and Microsystems

XXIV ciclo

Optical Characterization of Lithium Fluoride X-ray Imaging Detectors

Schirin Heidari Bateni

Tutors:
Prof. Fabrizia Somma
Dr. Rosa Maria Montereali
Coordinator:
Prof. Giuseppe Schirripa Spagnolo

February 2012

To my parents
Marlies and Farrokh Heidari Bateni

Acknowledgements

I would like to thank Prof. Fabrizia Somma, Dr. Rosa Maria Montereali and Dr. Francesca Bonfigli for their dedicated support of the present thesis. My profound thanks also to Prof. Gaetano Assanto for the two years under his guidance and to Dr. Doriano Brogioli for his support. Thank you for scientific, technical and personal contributions to Dr. Maria Aurora Vincenti and Stefano Libera. I would like to thank Dr. Enrico Nichelatti, Dr. Massimo Francucci, Dr. Pasquale Gaudio and Dr. Ivan Lupelli for their scientific contributions and the colleagues from the synchroton source ANKA for the fruitful collaboration. Thank you also to Paolo Aloe for his contributions. And finally, I would like to thank my family for their support.

Abstract

X-ray microscopy of biological samples is one of the main applications of imaging which plays an important role in Life Sciences [1]. The diffusion of this technique needs the development of compact laboratory x-ray microscopy systems. Important technological issues are the reduction of x-ray source dimensions, the improvement of x-ray optics and the development of new x-ray imaging detectors.

Several features, i.e. very high spatial resolution over a large field of view, large dynamic range, versatility and simplicity of use, make novel solid state detectors based on LiF very attractive as imaging plates for x-ray microscopy applications. Promising results for x-ray contact microscopy using LiF imaging detectors with a resolution close to a few hundred nanometer and large dynamic range have been obtained for various soft [2] and hard [3] x-ray sources. These innovative LiF imaging detectors are based on the optical reading of photoluminescence (PL) emitted by electronic defects (known as CC) induced by ionizing radiation in LiF crystals or thin films.

In the present thesis a set of samples was irradiated with hard x-rays (6-40 keV) at the TopoTomo beamline of the synchroton source ANKA, other sets with soft x-rays generated by a laser plasma souce.

The crystals irradiated at the synchroton source show intense PL signals of the aggregated F_2 and F_3^+ centres in the visible spectral range due to a high x-ray attenuation length. The optical response of a series of uniformly irradiated samples has been investigated as

function of the irradiation dose by varying the irradiation time. Crystal and thin film LiF detectors show a linear PL response covering two decades for both types of aggregated defects in the investigated experimental conditions. Even for x-ray imaging experiments on thin film exposure times in the order of 1 s are sufficient.

The z-scan technique of the CLSM has been used to study the spatial distribution of the CC in the coloured volume and a comparison between the simulation of the deposited energy density and PL signal profiles obtained along opposing directions has been performed.

LiF imaging detectors are ideal for contact microscopy with table-top x-ray sources, in particular for in vivo imaging experiments with laser plasma sources in single shot. These soft x-ray sources have intense emission in the water window (280-530 eV).

A study of the performance of thin film detectors irradiated at the TVLPS as function of growth parameters and irradiation conditions has been performed. In contact imaging experiments a resolution down to 630 nm has been obtained. To obtain an even higher resolution it is necessary to optimize the contact between samples and detector developing an appropriate sample holder. Thin films on silicon substrate exhibit a larger PL response than films on glass substrate mainly due to the higher reflectivity of the silicon substrate. Finally the high dynamic range obtained for LiF thin films allowed to perform an imaging test estimating the thickness of a flying insect wing.

Author's Bibliography

The following bibliography lists all publications of the author during research regarding the PhD degree, separated in two sections: the publications closely related to research regarding the PhD degree and marginally related or unrelated publications published in the same period.

Publications regarding PhD research

F. Bonfigli, R.M. Montereali, P. Gaudio, I. Lupelli, M. Richetta, S. Heidari Bateni and F. Somma, Optical microscopy and spectroscopy for readout and characterization of lithium fluoride X-ray imaging detectors, in Fotonica 2011, 13 Convegno Nazionale delle Tecnologie Fotoniche, Genova, 9-11 May 2011, ISBN 9788887237122, p.29, B1_5

S. Heidari Bateni, F. Somma, F. Bonfigli, A. Lai, R.M. Montereali, M.A. Vincenti, E. Nichelatti, P. Gaudio, I. Lupelli, M. Francucci, M. Richetta, Risposta di rivelatori a film sottile di fluoruro di litio per microscopia-X a contatto con una sorgente laser plasma, XCVII Congresso Nazionale Società Italiana di Fisica, L'Aquila, 26-30 settembre 2011, p.116

F. Bonfigli, T. Baumbach, A. Cecilia, S. Heidari Bateni, D. Pel-

liccia, F. Somma, P. Vagovic, E. Hamann, M.A. Vincenti and R.M. Montereali, First white beam X-ray imaging experiments with lithium fluoride detectors at the TOPO-TOMO beamline of the ANKA synchrotron, 3rd ANKA/KNMF Joint Users' Meeting, Karlsruhe, 13th-14th October 2011, p.88

S. Heidari Bateni, F. Bonfigli, A. Cecilia, D. Pelliccia, F. Somma, M.A. Vincenti, R.M. Montereali, Optical characterization of lithium fluoride detectors for broadband X-ray imaging, 2nd International Conference Frontiers in Diagnostic Technologies, Frascati, 28th-30th November 2011, p.78

F. Somma, F. Bonfigli, S. Heidari Bateni, A. Cecilia, T. Baumbach, D. Pelliccia, M.A. Vincenti and R.M. Montereali, Investigation of color centers distribution in x-ray irradiated LiF crystals by confocal fluorescence microscopy, Proc. 4th International Conference on Luminescence and its Applications, ICLA2012, Hyderabad, India, 7th-10th February 2012, ISBN-81-6717-806-5, p.14

Other publications

E. D'Asaro, S. Heidari-Bateni, A. Pasquazi, G. Assanto, J. Gonzalo, J. Solis, and C.N. Afonso, Interaction of self-trapped beams in high index glass, Opt. Express 17, 17150-17155 (2009)

E. D'Asaro, A. Pasquazi, S. Heidari-Bateni, and G. Assanto, Interaction of Spatial Solitons in a High-Index Glass, in Nonlinear Photonics, OSA Technical Digest (CD), Optical Society of America, 2010, paper NMD3

Contents

List of Figures

List of Tables

List of Acronyms

ANKA	Ångströmquelle Karlsruhe
AH	alkali halide
CC	colour centre
CCL	colour centre laser
CLSM	confocal laser scanning microscope
cw	continuous wave
DFB	distributed feedback
dof	degrees of freedom
EUV	extreme ultraviolet
EUVL	extreme ultraviolet lithography
FWHM	full width half maximum
GL	gray levels
gof	goodness of fit
HT	high temperature

IR	infrared
LiF	lithium fluoride
LNT	liquid nitrogen temperature
LT	low temperature
NA	numerical aperture
NEXAFS	near edge x-ray absorption fine structure
NIR	near infrared
OD	optical density
OPO	optical parametric oscillator
OSL	optically stimulated luminescence
PH	pinhole
PL	photoluminescence
PMMA	polymethyl methacrylate
PMT	photomultiplier tube
rms	root-mean-square
RT	room temperature
SEM	scanning electron microscope
SHI	swift heavy ion
Si	silicon
SNOM	scanning near-field optical microscope

STE	self-trapped exciton
SXCM	soft x-ray contact microscopy
TEM	transmission electron microscopy
TVLPS	Tor Vergata laser plasma source
WW	water window
XANES	x-ray absorption near edge structure
ZPL	zero-phonon line

Chapter 1

Motivations

Currently one of the major challenges of x-ray technology is about exploring and understanding the microscopic world, with new areas of research in the development of high-resolution x-ray microscopy instruments and techniques. X-ray microscopy of biological samples is one of the main applications of imaging which plays an important role in Life Sciences [1]. The diffusion of this technique needs the development of compact laboratory x-ray microscopy systems. Important technological issues are the reduction of x-ray source dimensions, the improvement of x-ray optics and the development of new x-ray imaging detectors.

Several features, i.e. very high spatial resolution over a large field of view, high dynamic range, versatility and simplicity of use, make novel solid state detectors based on LiF very attractive as imaging plates for x-ray microscopy applications in the fields of material science, characterization of intense x-ray sources, and biology, even for in vivo specimens [5]. Among radiation sensitive materials exhibiting active optical properties, LiF, in the form of bulk and film, is of particular interest because it is almost not hygroscopic and can host, even at RT, stable laser active CC that emit light in the visible and in the

near infrared spectral range under optical excitation [8]. Promising results in x-ray contact microscopy experiments have been obtained for various soft [2] and hard [3] x-ray sources by using LiF imaging detectors reaching a resolution close to a few hundred nanometers and high dynamic range. These innovative LiF imaging detectors are based on the optical reading of visible PL emitted by electronic point defects known as CC locally induced by x-ray radiation during the exposure process. In particular, the F_2 and F_3^+ aggregated defects have almost overlapping absorption bands peaked at about 450 nm, often called M band, and broad emission bands peaked at 670 nm and 535 nm, respectively [9, 10]. By using standard and advanced optical microscopes in fluorescence mode, such as Confocal Laser Scanning Microscope (CLSM) or scanning near field optical microscope, it possible to obtain PL images with micrometric [3] and nanometric [11] spatial resolution, respectively. The broad absorption and emission bands of the CC in LiF, located in the visible, allow the use of standard optical sources for blue light pumping and efficient readout methods. The intensity of the PL signal is locally proportional to the transparency of the specimen placed in contact with the LiF detector surface during the x-ray exposure.

Primary and aggregated defect formation is complex and depends on the selected ionizing radiation and on the irradiation conditions, such as particle flux and energy, exposure time, irradiation temperature, etc. [12, 13]. Moreover, these processes also depend on the structural and morphological properties of the detector, e.g. LiF single crystals or polycrystalline thin films [8, 14].

In the present thesis, two sets of LiF samples have been studied as x-ray imaging detectors: one set was irradiated with polychromatic hard x-rays at the TOPO-TOMO beamline of synchrotron light source Anka, another one was exposed to soft x-rays produced by a laser plasma source.

For irradiation at higher x-ray energies in the synchrotron light

source, characterized by a high attenuation length and a quite large dose interval, covered with the variation of the exposure time, the detector response in absorption and PL of a series of coloured LiF crystals as a function of exposure times was investigated. For the first time x-ray imaging tests on LiF crystals and films performed with this polychromatic x-ray source were analysed. Finally, as the CC spatial distribution along the radiation penetration direction is not homogenous, the CLSM technique was exploited to investigate the relationship between the detected PL signal and the CC distribution along the thickness in the x-ray irradiated crystals containing CC at different concentrations.

LiF imaging detectors are ideal candidates for contact microscopy with tabletop x-ray sources, also for in vivo imaging in single-shot experiments with a laser plasma source. These polychromatic x-ray sources have intense emission in the water window (280-530 eV), where a large difference in water and carbon absorption allows the acquisition of naturally contrasted x-ray images of biological objects. At the TVLPS, we compared LiF crystal and thin film detector performances for different growth parameters, such as film thickness and substrate type, and irradiation conditions (target material, etc.) in single-shot experiments. In combination with imaging experiments, these investigations are fundamental in order to obtain quantitative information from soft x-ray microradiography and microscopy.

Chapter 2

State of the Art

2.1 Introduction

X-ray contact microscopy was invented more than a hundred years ago as the first technique for x-ray microscopy[1, 15]. X-ray imaging detectors have either high resolution or large dynamic range while LiF based ones combine both these characteristics on a wide field of view. LiF is a versatile material, with many applications which has been studied extensively. This chapter gives an overview of the state of the art in x-ray contact microscopy (section 2.2), x-ray imaging detectors (section 2.3) and LiF (section 2.4).

2.2 X-ray Contact Microscopy

Soon after the discovery of x-rays by Röntgen in 1895 [1, 16] they were applied to the study of biological samples [1, 15, 17]. Projection microscopy was invented in 1951 [1, 18]. In 1956 the enlargement of microradiographies on silver halide films with the optical microscope was replaced by the reading of surface relief patterns with the electron

microscope [19]. This development was followed in 1976 by the application of photoresists in contact microscopy [1, 20, 21]. After invention of the zone plate transmission microscope in 1976 [1, 22], the use of synchroton sources in x-ray microscopy started in 1977 [1, 23, 24]. The potential of the WW for imaging of living cells with x-ray microscopy was recognized in the 1980s [25, 26]. Since the 1980s there have been various improvements in x-ray contact microscopy, e.g. the use of pulsed x-ray sources for shorter exposure times and in vivo imaging as well as improved read-out methods with TEM and atomic force microscopy ([19] and references therein).

Visible light microscopy achieves wavelength-limited spatial resolutions up to 250 nm, and many biological specimens have to be stained for imaging which may induce changes in the sample [25]. TEM achieves a higher resolution than x-ray microscopes, but the samples need extensive preparation and can not be imaged in vivo in their natural environment [25]. There are various techniques for x-ray microscopy. X-ray contact microscopy was the first technique to be explored and remains the simplest one up to present days [1]. The sample is irradiated in direct contact with a detector, then the resulting microradiography is enlarged. Projection x-ray microscopy uses a very small x-ray source to produce a magnified shadow image [27]. In transmission x-ray microscopy, analogous to visible light transmission microscopy, an objective lens, usually a zone plate, produces a magnified image of the sample [1, 27]. In scanning x-ray microscopy the x-ray beam is focused to a microprobe which is used to scan the sample point by point [1, 27]. Incoherent light is used in x-ray contact microscopy and transmission x-ray microscopy, coherent light for scanning x-ray microscopes [1].

XANES or NEXAFS near edge resonances give information about the chemical environment of the atoms since the electrons are excited to energy levels close to the vacuum which are influenced by the nature of the chemical bonds [1]. A map of the element distribution can

be created by the combination of two images, one taken below the absorption edge and the other above [1].

SXCM is a suitable technique for imaging the ultrastructure of complex biological samples without need for dehydration [28, 29]. Using a laser plasma source short exposure times below the time scale of radiation damage to the sample can be achieved [5, 28, 30]. With the development of table top x-ray sources images can be acquired in biological laboratories [31]. Samples such as roundworms, green algae, yeast and Leydig cells, human red blood cells and sperm have been imaged successfully [28, 29, 32, 31]. SXCM is still largely qualitative [31], a characterization of the single shot and the corresponding image quality is started in this work.

2.3 X-ray Imaging Detectors

X-ray photographic films have a large field of view (many cm^2) and a reasonably high spatial resolution (a few micrometers) [33, 2]. They are very sensitive, but the dynamic range is very low [33, 2]. The dynamic range is the interval between the lowest detectable optical density and saturation [33]. In addition, x-ray photographic films require a development procedure which leads to low duty cycles, i.e. only a small fraction of time needed for the realization of an image is due to x-ray exposure and read-out [33]. Photographic films disappear from the market because of limited dynamic range, nonlinear response and absence of digital output [34].

In photoresists, x-ray absorption causes breaks in the polymer chain [19, 28, 30]. The lower molecular weight in the irradiated areas yields a higher solubility in chemical developer [19, 28, 30]. Development produces a relief map with dose-dependent height which is read out by atomic force microscopy. PMMA has a high spatial resolution of about 10 nm, but its use is limited to large national facilities due to

its low sensitivity [29]. PMMA is especially insensitive to hard x-rays and used mainly for soft x-ray experiments [3]. In addition, a development process is necessary and the atomic force microscope employed for read-out has a field of view of only a few tenths of μm^2 [35].

X-ray CCDs, on the other hand, have high dynamic range, high sensitivity and simple read-out, but a field of view of only 1-10 cm^2 and a spatial resolution limited by the pixel size [2]. This characteristic necessitates the use of FZP with monochromatic sources and, due to the need for high fluence to reduce statistical noise, favours the expensive use of synchroton sources [2]. CCDs with very high spatial resolution can not be used with laboratory source due to intensity considerations [3].

A pixel detector can be hybrid or monolithic [34]. The hybrid pixel detector consists of two chips. The detector chip is a semiconductor diode with a pixelated front and a common contact on the backside. Separate read-out electronics for each pixel are provided by the read-out chip. The main advantage of this architecture is the possiblity to process single particles independently. In addition, it is possible to combine the read-out chip with sensors of different materials to detect any type of ionizing radiation. Monolithic chips, on the other hand, are restricted to silicon. The limitations of hybrid pixel detectors are the same as for monolithic CCDs, in particular a very low spatial resolution.

2.4 Lithium Fluoride

2.4.1 Material Properties and Radiation Effects

AH have been studied since the late 19th century; today they figure among the best-known materials and are used as model materials for more complex media [36, 37, 38, 4]. Due to its wide optical gap LiF is

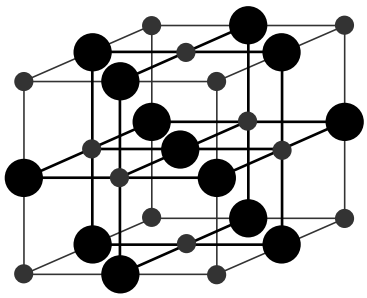

Figure 2.1: fcc structure of LiF.

especially suitable for investigation of the formation of electronic defects [39, 40]. In addition, CC in LiF show high physical and chemical durability as well as high photothermal stability, quantum efficiency and optical gain [41, 42]. Thus generation and study of CC in LiF have been pursued since the late 19th century [37]. Currently LiF is a versatile medium in miniaturization of optical components in new materials and configurations for higher compatibility with integrated optical technologies [43].

LiF is an AH with the typical ionic structure (fig. 2.1). Li^+ and F^- have the smallest radii among alkali and halide ions of 0.06 and 0.136 nm, respectively, and their distance of 2.013 Å is the shortest among AH [8]. Thus a high CC density and high spatial resolution can be achieved in LiF [2]. The large difference in electronegativity induces large Coloumb forces which in turn yield a high melting point of 848.2°C and the largest bandgap of all dielectrics. The bandgap of more than 14 eV renders the material an insulator transparent in a large spectral interval between about 120 nm and 7 μm [44]. Due to the directed orientation of its ionic bonds LiF may be exposed to high irradiation doses without amorphizing [45, 46]. LiF is hard and non-

hygroscopic (the solubility of NaCl in water is more than 300 times higher), with a Knupp hardness of 99 kg/mm^2 and a solubility of 0.134 g per 100 g water at 25°C [47, 8]. The refractive index (1.396 at 445 nm, [48]) is one of lowest among dielectric materials [47].

Under low-energy electron irradiation apart from CC formation desorption, dissociation and sputtering have been observed as well [49]. For 800 eV argon ion sputtering smoothening and appearance of ripples with a mean height of 2 nm and a period of 30 nm on the film surface was observed [50]. This process has been explained as the result of the competing mechanisms of ion erosion and surface diffusion [50]. After irradiation with 15 MeV gold ions a 150% increase in hardness was found with repect to the uncoloured LiF crystal [46]. This hardening is mainly due to dislocations and defect aggregates [46]. Another effect of SHI irradiation is a decrease of the grain size in LiF films due to fragmentation [38], also responsible for hardening since it increases the number of grain boundaries [46, 38].

After investigation of AH films in the early 1960s and of LiF crystals in the 1980s, study on LiF thin films began with the 1990s [36, 51]. LiF thin films were deposited on amorphous substrates to investigate spontaneous growth as function of substrate temperature during growth. The films are polycrystalline (distribution of x-ray diffraction signals about 15° around the peak) and display sharp edges and smooth surfaces [51]. The (111) planes are nearly perpendicular to the substrate surface in the thin films grown at a temperature smaller than or equal to 200°C, while for films grown at temperatures larger or equal to 250°C the (100) plane is nearly parallel to the substrate surface [51]. While the lattice parameter is equal to that of LiF crystals at 4.02 Å, the refractive index for the thin film grown at 43°C (1.335 in the wavelength interval between 500 and 800 nm) is lower than the refractive index of 1.388 obtained for LiF crystals and thin films grown at higher temperatures [51]. The real part n of the refractive index $(n - ik)$ of LiF thin films is always lower than that of bulk samples

[52]. The presence of voids reduces the compactness of the film and consequently the refractive index. Since high temperature films are compacter the refractive index increases with the temperature during growth. It decreases with increasing film thickness [52]. The extinction coefficient k is about $5 \cdot 10^{-4}$ [52].

In LiF thin films on amorphous substrates the (100) plane approaches the direction parallel to the substrate surface with rising substrate temperature during growth [53]. The dimension of the globular grains for high temperature films is about 250 nm, for low temperature it is ∼150 nm. The refractive index increases with increasing temperature, up to 10% difference can be achieved with variations of the temperature [53]. The refractive index is largely dependent on density which in turn is determined by the film structure [53, 54]. A LiF thin film grown on crystalline Si substrate, on the other hand, is oriented with the (100) planes parallel to the substrate surface [55]. Though it displays single crystal texture the growth is not epitaxial due to a thin native oxide layer on the substrate surface. A SEM micrograph confirms a smooth surface with a grain dimension of about 250 nm [55].

2.4.2 Colour Centres

CC were reported as early as 1830 in CaF_2 [56, 57]. Systematic studies started in the 1920s [56, 58] and excitons were first described in the 1930s [59, 60]. In the 1950s and 1960s the role of excitons in CC formation was explored both experimentally and theoretically [56, 61, 62, 63, 64]. An F^- ion forms a molecule with a neighbouring ionized F atom [65, 44]. If this self-trapped hole captures an electron in an excited state it becomes an STE. The STE may decay via luminescence, lattice vibrations or formation of Frenkel pairs, i.e. an interstitial F^- ion (I centre) or a F atom (H centre) and a vacancy (α

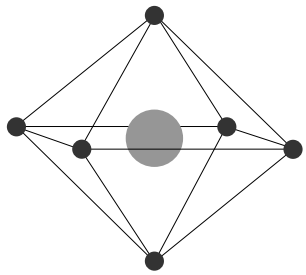

Figure 2.2: The F centre is an anion vacancy which has captured an electron, shown with six Li^+ ions as closest neighbours.

centre) or a vacancy which has captured an electron (F centre, fig. 2.2, [56, 66, 44]). The hole centres are orders of magnitude more mobile than the electron centres [45]. Hole and electron centres have to be at least five interatomic distances apart to form a stable Frenkel pair [66, 67, 68, 69]. The lifetime of the exciton has to be long enough and the energy of the excited state larger than that needed for defect formation [56]. The STE relaxe to Frenkel defects in 0.1-10 ps [56, 70, 71]. In AH radiation damage occurs preferably in the halogen sublattice [45]. F_2 centres (fig. 2.3 a) are formed when a diffusing vacancy units with an F centre and captures an electron [65]. Generation of F_3^+ centres (fig. 2.3 b) takes place via union of a vacancy with an F_2 centre or of a diffusing F centre with an F_2^+ centre [65]. The CC dimension is less than 1 nm [3].

Farge presented a model for colouration kinetics in AH based on LiF in 1969 [72]. The model assumes a constant number of traps for hole centres which results in a two-stage colouration curve. The extrinsic first stage is steep and dependent on impurities and dislocations, the intrinsic second stage characterized by a slower colouration.

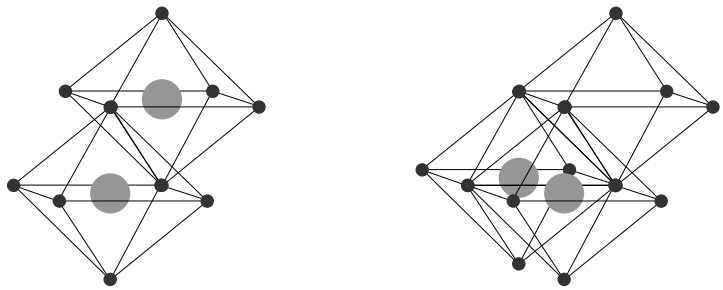

(a) (b)

Figure 2.3: F_2 a) and F_3^+ b) aggregate defects.

In very pure samples the first stage is not observed and the F centre density increases with the square root of the irradiation time. Saturation of the extrinsic colouration occurs when the mobility of vacancies suffices for recombination with interstitial I centres. Saturation follows an exponential law as the extrinsic colouration rate decreases with the number of available saturable traps [72, 73]. In 1973 Agulló-López and Jaque introduced the formation of interstitial clusters as non-saturable traps and a corresponding third stage in the colouration curve for NaCl [74, 75]. Thévenard et al. presented their model of CC formation in LiF for bombardment with high-energy particles in 1977 [76].

CC can be induced by irradiation with x-rays, α-, β-, and γ-radiation as well as protons, neutrons and ions [44]. Uniform colouration along the sample thickness is achieved with γ-rays. Protons, α-rays and ions yield intense colouration of a small surface layer, MeV electrons a uniform colouration along a few millimeters, while for keV electrons colouration is superficial and its depth may be controlled

Defect	Absorption peak [eV]	Absorption FWHM [eV]	References
F	4.96	250	[77]
F_2^+	1.92	0.433	[8, 78]
	1.97	0.434	[79, 80]
F_2	2.79	0.16	[8, 78, 81]
F_2^-	1.29	0.21	[10]
F_3^+	2.77	0.29	[8, 78, 81]
$F_3(R_1)$	3.92	0.52	[80]
$F_3(R_2)$	3.31	0.66	[80]
$F_3^-(R_1)$	1.88		[82]
$F_3^-(R_2)$	1.55	0.185	[10]
$F_4(N_1)$	2.40	0.21	[80]
$F_4(N_2)$	2.26	0.22	[80]
$F_4 - like$	1.91	0.19	[83]

Table 2.1: Defects in LiF and the parameters of their main absorption bands.

Defect	Emission peak [eV]	Emission FWHM [eV]	References
F_2^+	1.36	0.29	[8, 78]
F_2	1.83	0.36	[8, 78, 81]
F_2^-	1.11	0.17	[10]
F_3^+	2.29	0.31	[8, 78, 81]
$F_3^-(R_2)$	1.38	0.331	[10]
$F_4 - like$	1.69	0.16	[83]

Table 2.2: Defects in LiF and the parameters of their main emission bands.

by the chosen energy. The colouration achieved with x-rays is depth-dependent. For charged particles, spatial resolution is limited by beam enlargement due to charge effects in the insulating material [43]. In the case of low-energy electrons scattering has to be taken in consideration as well [43]. For x- and γ-rays, on the other hand, the spatial resolution is limited by photoelectron blurring [84]. EUV light ($20 < h\nu < 300$ eV) and soft x-rays ($0.3 < h\nu < 8$ keV) have the combined advantages of neutrality (no charge effects in insulating materials), limited penetration (limited photoelectron blurring), low scattering cross section (limited beam spreading) and short wavelength [84]. It is not possible to colour LiF via additive colouration (thermo-chemical reduction, [77, 85, 81, 4]).

Tables 2.1 and 2.2 show some of the defects found in LiF with the parameters of their absorption and emission bands. According to the hydrogenoid model of the F centre in a dielectric material the F centre emission band should be centred at about 900 nm overlappping with

the emission of the F_2^+ centres [4]. Since all samples contain at least a few F_2^+ centres which absorb also at ∼250 nm F centre emission has not yet been verified. In LiF CC are stable at room temperature and their emission bands fall in the visible and NIR spectral interval [86]. CC have a high transition oscillator strength and an optical activity with a quantum efficiency close to one [39, 37, 84, 87, 88].

The majority of defects, apart from F centres, are F_2 and F_3^+ centres whose absorption forms a broad band because of phonon interactions with the lattice [87, 88]. For laser applications it is useful to destroy one of the two aggregate defects. This is achieved by annealing or photoionization. F_3^+ centres are stable up to 125°C, F_2 centres up to 200°C [89]. Thus a population consisting mainly in F_2 centres is achieved [90]. Irradiation with a 308 nm XeCl laser, on the other hand, converts F_2 centres to F_2^+ and F_3 to F_3^+ centres [90, 89]. Under LT irradiation more F_3^+ than F_2 centres are formed as well, and the concentration of complex aggregate defects decreases due to reduced mobility of the interstitials [90, 91, 92, 69]. For RT irradiation with 5 MeV electrons the ratio between F_2 and F_3^+ centres is about 1 and constant as function of the irradiation dose [40]. In another experiment low-energy electron irradiation of different LiF films produced a majority of F_2 centres [52]. For irradiation at 213 K there are more than twice as much F_3^+ centres as F_2 centres and the concentration of other complex centres is decreased [40]. Irradiation with 5 MeV electrons also reduces the concentration of complex defects with respect to irradiation with γ-rays [92], though irradiation with γ-rays produces more F_3^+ centres [93].

A power-dependent quenching has been observed for F_3^+ centre PL [94]. The quenching is reversible in the dark, with long characteristic times suggesting the involvation of singlet-triplet transitions. After an equilibrium of the singlet transitions has been achieved on a fast timescale triplet transitions take place on a slower timescale. Thus the use of F_3^+ centres in CCL is limited to pulsed operation.

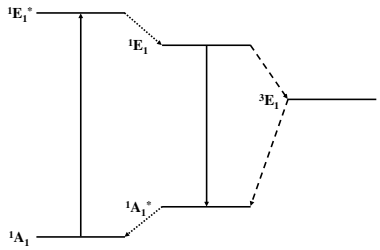

Figure 2.4: F_3^+ centre energy-level diagram [4]. The four-level cycle of e.g. F_2 centres consists in the radiative (solid lines) and relaxation transitions (dotted lines). The dashed lines are radiationsless transitions to and from the triplet state.

F_2 centres have a four level, F_3^+ centres a five level optical cycle including the metastable triplet state (fig. 2.4, [39, 90, 37, 4]).

For concentration quenching of F_2 centre PL, on the other hand, singlet-triplet transitions with a slow timescale can be excluded because low-concentration PL decay times are identical to the lifetime of the excited state [91]. Instead there is an energy transfer to F_2^+ centres whose absorption band overlaps with the F_2 emission band.

Colour centre formation efficiency is higher in polycrystalline films and depends on the deposition parameters such as film thickness, substrate temperature and deposition rate [52]. Surface-to-volume ratio, void presence and preferred orientation of the crystallites are influenced by these parameters. The F_2 centre concentration is two to five times higher in LiF films on glass substrate than it is in LiF crystals, and the films grown at a higher temperature display a higher defect density [52]. In another experiment thin film PL is reported 10 times higher than the bulk signal [2].

2.4.3 Applications

LiF is known for its applications as dosimeter material [93, 95, 96] and in antireflection coatings [55, 97].

LiF is a promising candidate for miniaturization of optical components for integrated circuits [98, 99]. The increase in the real part of the refractive index in the spectral interval of CC emission connected with CC formation permits the writing of waveguides and other structures with periodic modification of refractive index and gain [84]. In EUVL optical lithography is extended to shorter wavelengths. This technique allows writing of CC in LiF with micrometric resolution [100]. Photoluminescent lines and dots were written in LiF utilizing a focused soft x-ray beam, a soft x-ray laser or ion bombardment [43, 84, 50]. Photorefractive gratings are often used to reduce linewidth and threshold of laser emission [101]. The LiF crystals with periodic lithium-enriched light-emitting patterns have possible applications as substrates for deposition, ordering and characterization of other materials as well ([50] and references therein). Permanent Bragg gratings with different periodicity were recorded in surface coloured LiF crystals by UV bleaching with a phase-mask interferometer [101]. Interferometric encoding of low-dimensionality gratings with a soft x-ray laser has been achieved as well [102]. With a 12 keV electron beam an increase of the refractive index by $5 \cdot 10^{-3}$ was obtained in a single-mode waveguide [103, 104]. While irradiation with MeV He ions produced a multimode waveguide, no propagation was observed for carbon irradiation due to the increased presence of complex aggregate centres [105].

LiF-based microcavities serve the dual purpose of studying the interaction between light sources and vacuum field fluctuations and of exploring new possibilities for active optical components in integrated circuits [106, 107, 108]. In microcavities the interaction of the radiating dipoles and the cavity field changes the spontaneous emission

properties [106]. In LiF-based microcavities spectral narrowing, increase of the peak intensity, spatial redistribution of the radiation and a shortening of the lifetime have been observed [106, 107, 108].

Due to the four-level optical cycle, CCL belong to the solid state vibronic laser family [36]. They are characterized by the possibility to obtain population inversion even with low-power pumping [36]. F_2^+, F_2, F_2^-, F_3^+ and F_3^- centres have been utilized to create CCL operating at 0.84-1.12, 0.65-0.74, 1.09-1.26, 0.51-0.57 and 0.86-1.02 μm, respectively ([90] and references therein). An example is a tunable F_2 or F_3^+ DFB CCL fabricated with IR femtosecond laser pulses in a LiF single crystal [42, 109]. This technique might be applied to the fabrication of integrated optical circuits as well.

The same spectroscopic properties as in LiF crystals were found in single-crystalline LiF fibres which have a potential application in miniaturized active optical devices [39]. F_2^- centres emit in the spectral interval used for optical communications [39].

ZPL are electronic transitions taking place without phonon interaction with the lattice and yielding narrow peaks in the LT emission spectra [110]. Holes can be burned into ZPL by photoionization of the participating centres. Spectral hole burning yield information about ZPL and is utilized for optical data storage [111]. Spectral hole burning has been achieved for F_2, F_2^- and F_3^- centres [111, 112, 113].

2.4.4 LiF X-ray Imaging Detectors

The fast progress in the development of laboratory x-ray sources as well as large scale facilities leads to new developments in the fields of x-ray microscopy and tomography [3]. In particular, improvements of the key elements, i.e. x-ray source, optics and detectors, have been achieved [3]. LiF is proposed as detector for the most straightforward technique: lensless imaging in absorption contrast [3].

LiF x-ray imaging detectors have many advantages, among them

simplicity of use, a large dynamic range and high spatial resolution on a large field of view. In addition they are inexpensive. It is possible to recycle thin film detectors by heating them up to 500°C, but the production with an evaporator is too inexpensive to make this worthwhile. The LiF detector does not need a development procedure and due to the large optical gap screening from visible light is unnecessary. The microradiography is stable for years with a simple read-out procedure [111]. The LiF detector does not need electronic supply and is vacuum compatible [2]. A drawback is the relatively low sensitivity [3]. This problem can be resolved by appropriate choice of detector properties and irradiation conditions [3]. The final resolution is determined by the read-out instrument which can be e.g. a CLSM or a SNOM.

The material properties determine the colouration efficiency and thus the sensitivity of the detector [35]. Colouration efficiency is defined as the ratio between defect density and irradiation dose [47]. For irradiation with EUV radiation and soft x-rays generated by an excimer laser on a tantalum or copper target the minimum dose to obtain a signal distinguishable from the scattering noise of the CLSM is 1 mJ/cm^2 [47]. A resolution of less than 100 nm may only be achieved with fluences from about 100mJ/cm^2 upwards due to statistics of the photon density distribution [47].

Fig. 2.5 shows the working principle of the LiF x-ray imaging detector [5]. For realization of a microradiography the sample and the detector are exposed to ionizing radiation, in our case x-rays. In contact microscopy the biological sample is put in direct contact with the LiF detector. The irradiated detector with the stored image dependent on sample thickness and x-ray absorption coefficient is then placed under a fluorescence microscope. F_2 and F_3^+ aggregate defects possess a broad common absorption band around 450 nm which can be excited by a mercury lamp or an argon laser at 457.9 nm. The readout process of LiF detectors consists of detecting the efficient photoluminescence of CC in the visible spectral range under blue light pumping. The in-

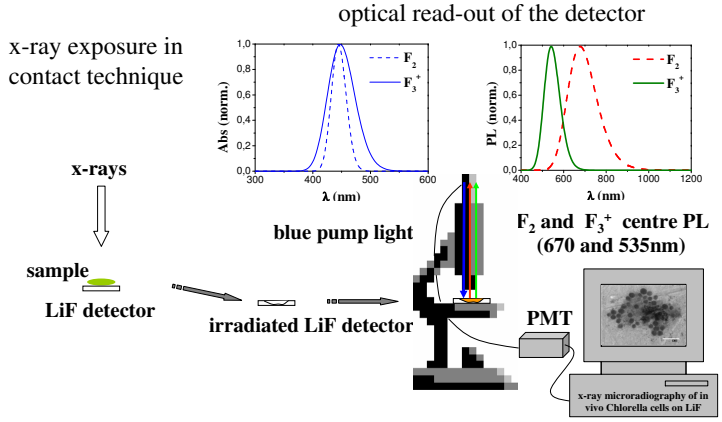

Figure 2.5: Working principle of LiF x-ray imaging detector [5].

tensity of the PL signal is locally proportional to the transparency of the specimen placed in contact with LiF surface during the x-ray exposure. In fig. 2.5 the digitized microradiography of in vivo Chlorella cells [5] the cells appear as dark areas where less centres have formed due to the absorption of the x-rays in the biological sample.

Chapter 3

Methodology

3.1 Introduction

Irradiation at a synchroton source yields a large PL signal due to the high attenuation length which allows to study the detector response on a large irradiation dose interval. On the other hand, single shot irradiation with a laser plasma source is ideal for soft x-ray in vivo imaging of biological samples due to the high photon flux, the high contrast in the water and carbon windows and the short irradiation time preventing damage to the samples [5, 1, 35, 25].

In this work we performed systematic investigations of detector performance as function of irradiation times, thin film characteristics and target material. This chapter deals with sample preparation and irradiations (section 3.2) as well as their optical characterization through optical absorption and PL measurements, as well as confocal laser scanning fluorescence microscopy (section 3.3).

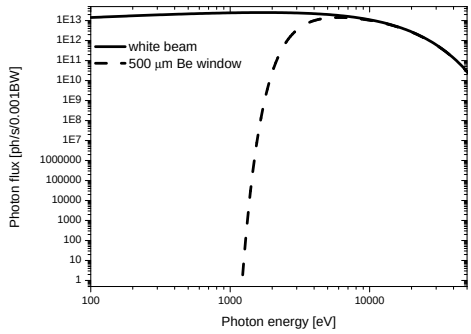

Figure 3.1: Spectral interval covered by the synchroton light source ANKA.

3.2 Preparation of LiF Samples

3.2.1 Irradiation at the Synchroton Source

In a synchroton charged particles are accelerated by high-frequency alternating electric fields. Magnetic fields which increase with increasing velocity of the particles keep them on a circular trajectory. The dipole magnets of the synchroton light source ANKA (Karlsruhe Institute of Technology) operate with a 1.5 T magnetic field. The synchroton source ANKA is characterized by an electron energy of 2.5 GeV and beam currents of 150-180 mA. The white beam covers a large spectral interval from less than 0.1 keV up to 40 keV with a critical wavelength of 2 Å (fig. 3.1). The TopoTomo beamline consists in two in-vacuum slits separated by a distance of 30 m. The exit window in the experimental hutch is a 500 µm beryllium window which cuts off the lower part of the spectrum with photon energies below 2 keV approximately (fig. 3.1, [114]).

The samples irradiated at the synchroton source ANKA are six (5x5x0.5) mm Macrooptica LiF crystals as well as a 1 µm thick LiF

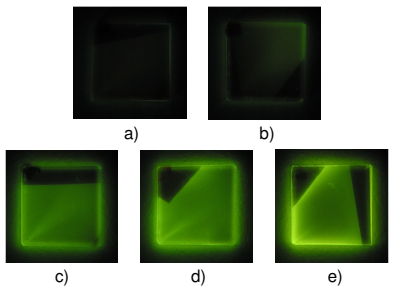

Figure 3.2: Five LiF crystals irradiated for a) 0.5 s, b) 1 s, c) 5 s, d) 10 s and e) 30 s at the synchroton source Anka under blue LED illumination.

thin film thermally evaporated on a glass substrate. Irradiation took place at RT. Five crystals were irradiated with a (6x8) mm beam and exposure times of 0.5, 1, 5, 10 and 30 s at a distance of 43.5 cm from the beam shutter. Fig. 3.2 shows these samples under blue LED illumination (450 nm). Due to attenuation in air, the spectral interval covered by the white beam impinging on the samples is between 6 and 40 keV. The other LiF crystal and the thin film were irradiated by a (800x800) µm beam with an Xradia test pattern inserted at a distance of 26 cm from the beam shutter. The test pattern consisted in a gold mask on a (500x500) µm Si_3N_4 window and was exposed for 1, 2, 2.5, 5, 10, 20, 30 and 60 s (fig. 3.3). Taking into account the attenuation of the beryllium window and the following propagation in air, the photon flux on the samples is estimated $2 \cdot 10^{13}$ph/s/mm^2.

The LiF thin films used in this work were grown from Merck suprapur LiF powder by physical vapour deposition at the GP20 SISTEC-Angelantoni evaporation facility at the ENEA C.R. Frascati by Dr. A. Vincenti ([115], fig. 3.4). Before the evaporation film thickness and

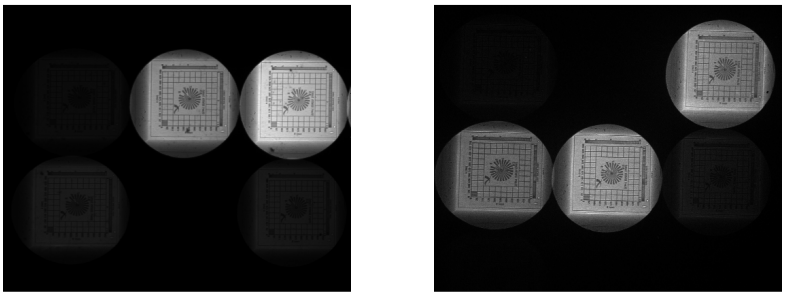

(a) (b)

Figure 3.3: LiF crystal a) and 1 μm LiF thin film b) with microradiographies of the Xradia test pattern irradiated with different exposure times under laser illumination at 457.9 nm.

evaporation rate are selected; the latter is controlled by an oscillating quartz crystal which changes weight and thus frequency with LiF deposition. The LiF powder is evaporated in vacuum from a crucible heated via Joule effect. If the evaporation is too fast the current in the crucible is decreased. A lamp behind the rotating sample holder heats the substrates to 300° in 90 minutes. The temperature is controlled by two thermocouples calibrated with a third one in contact with the substrates. The substrates are kept at 300° for an hour, then the evaporation takes place and the substrates should cool down in eight and a half hours to reduce thermal stress during cooling. Power on the crucibles, on the other hand, reaches 50% of the maximum power in 40 minutes and remains like that for 10 minutes to dispose with contaminations while the crucible is covered with a shutter. In another 10 minutes the power reaches 70% of the maximum value and remains like that for 3 more minutes before the crucible is uncovered. Evaporation starts at 80% of the maximum power.

Figure 3.4: GP20 SISTEC-Angelantoni evaporation facility at the ENEA C.R. Frascati.

3.2.2 Irradiation at the Soft X-ray Laser-Plasma Source

The TVLPS consists in a Nd:YAG/glass laser and a solid tape target in a vacuum chamber [116]. The light pulse from the Q-switched Nd:YAG oscillator with a maximum energy of 36 mJ is amplified in two Nd:YAG and two Nd:glass amplification stages. Both oscillator and first amplifier are equipped with two flash lamps, while the third amplifier is equipped with four. Maximum pulse energy at the exit of the first amplifier is 220 mJ, behind the second it is 781 mJ. Both amplifiers work with a repetition rate of 10 Hz. The third and fourth amplifier are pumped by six and eight flash lamps, respectively, and rise the pulse energy to a maximum of 3.94 and 10 J, respectively. These amplifiers work with an optimum repetition rate of one shot every four minutes. Two optical isolators are also part of the laser system. They are placed between oscillator and first amplifier as well as between the first and second amplifiers and consist in a 56.5° polarization plate and a Faraday rotator, followed by a $\lambda/2$ and another

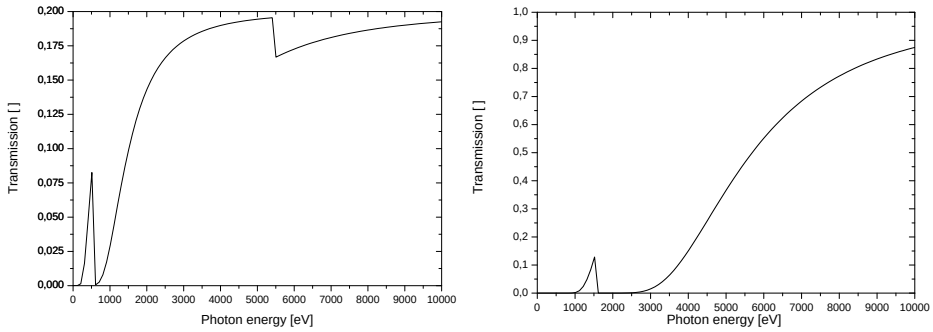

(a) (b)

Figure 3.5: Transmission spectrum of 0.5 μm vanadium filter on mylar mesh a) and 20 μm aluminium filter b).

56.5° polarization plate. The isolators prevent interaction between the amplifiers and damaging of the optics by retrodiffused radiation from the plasma. Energy of the x-ray radiation from the plasma is measured by a Quantrad PIN photodiode with a 300 nm Si input window, an active intrinsic region of 125 μm and a n^+ doped cathode. For irradiation with the yttrium target measurements were performed with a 0.5 μm vanadium filter on a mylar mesh in front of the PIN diode to evaluate the x-ray energy in the WW (fig. 3.5 a). For irradiation with the copper target, on the other hand, the measurements were performed with a 25 μm aluminium filter to evaluate the energy of the more penetrating x-rays with photon energies between c 1 and 1.5 keV (fig. 3.5 b). The spectra are due to Dr. I. Lupelli.

In the WW between the carbon and oxygen K absorption edges at 284 eV/4.3 nm and 540 eV/2.3 nm (fig. 3.6) there is a large difference of nearly an order of magnitude in the absorption of water and carbon which allows to obtain highly contrasted images, in particular

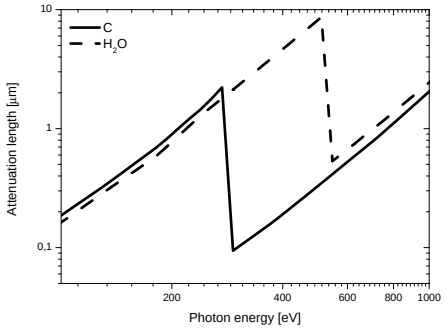

Figure 3.6: WW between carbon and oxygen K edges.

of in vivo organisms [1]. A natural contrast is obtained for imaging of cells since the cytoplasm is mainly water while other parts of the cell such as cellular wall, nucleus and organelles are mostly carbon [30]. The carbon window between 250 eV/5 nm and 280 eV/4.4 nm is characterized by high x-ray penetration in organic materials and 5-6 times larger differences in absorption which allow to distinguish between different organic compounds without staining [35]. The M series of yttrium is in the WW, while the L series of copper around 1000eV provides more penetrating x-rays [117]. The yttrium target displays a high conversion efficiency from laser radiation to x-rays in the WW [118], the copper target a high conversion efficiency to x-rays in the spectral interval between 1.3 and 1.55 keV [116]. Due to the high flux laser plasma sources are ideal for x-ray imaging [5]. The spectral characteristics are determined by target material and the size of the laser spot on the target [5]. In single shot the complete x-ray fluence is delivered during the pulse duration of about 30 ns. This method limits modifications of and damage to the sample [35, 25]. A vacuum dried mosquito wing was irradiated with 500 shots without showing distortions due to heating [35]. The time interval for radiation damage

to the sample is in the order of microseconds and movements of cells or organelles take place on a time scale larger than the irradiation time as well [5]. Thus single-shot irradiation with a laser plasma source is ideal for in vivo imaging.

The x-ray fluence F on the LiF crystals irradiated at the TVLPS was calculated by Dr. I. Lupelli from the University of Tor Vergata according to the following formula [116]:

$$F \cong \frac{V_x}{R_L} \frac{\tau_x}{S_{xrd}} \frac{1}{A_{exp} T_f}. \tag{3.1}$$

Here V_x is the amplitude of the x-ray pulse detected by an oscilloscope, R_L the load the PIN diode is connected to, τ_x the duration of the x-ray pulse, S_{xrd} the PIN diode responsivity and A_{exp} the sensitive area of the PIN diode. T_f is the transmittance of the filter in front of the PIN diode. The filters were a 0.5 µm vanadium filter on a mylar grating for the yttrium target and a 25 µm aluminium filter for the copper target. The 3 µm SiO layer on the PIN diode in the spectral interval between 200 and 600 eV and at 1.5 keV is taken into consideration as well.

The major part of the x-ray emission from a laser plasma source is due to bremsstrahlung of the free electrons decelerated in the electric field of the plasma ions [119]. This spectrum is described in first approximation as black-body radiation, though Planck's law actually requires an equilibrium state between matter and emitted radiation [119]. The photon flux due to bremsstrahlung $L(\nu, T)$ [119] can easily be transformed into functions of the photon energy E and wavelength λ:

$$L(E, T) = \frac{2E^3}{h^3 c^2} \frac{1}{exp\left(\frac{E}{kT} - 1\right)} \frac{\Delta E}{E} \tag{3.2}$$

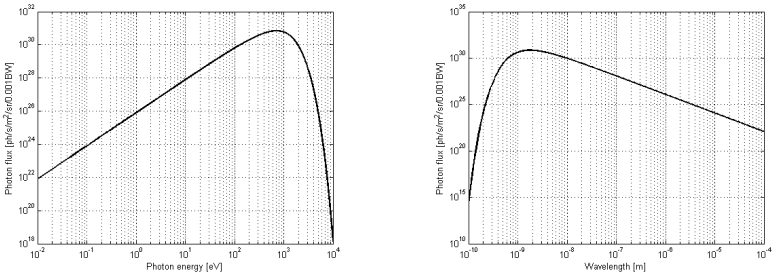

(a) (b)

Figure 3.7: Photon flux due to bremsstrahlung from a laser plasma source for an electronic temperature kT of 250 eV, a) as function of photon energy and b) as function of wavelength.

and

$$L(\lambda, T) = \frac{2c\lambda}{\lambda^4} \frac{1}{exp\left(\frac{hc}{\lambda kT} - 1\right)} \frac{\Delta\lambda}{\lambda}, \tag{3.3}$$

with $d\nu = dE/h$ and $d\nu = cd\lambda/\lambda^2$. Here T is the temperature, h the Planck constant, c the velocity of light in vacuum and k the Boltzmann constant. Fig. 3.7 a) and b) shows the photon flux of the bremsstrahlung calculated for an electronic temperature kT of 250eV [116] as function of photon energy and wavelength, respectively. Due to the introduction of the relative bandwidth $\Delta E/E$ and $\Delta\lambda/\lambda$ the maximum of both spectra is at 700 eV (λ=1.65nm) [119].

Fig. 3.8 shows the x-ray attenuation length in LiF for photon energies from 30 to 30000 eV [6] with the K absorption edges of Li and F at 54.7 and 696.7 eV, respectively [117]. The M_{III} edge of yttrium at 300 eV [120] and the characteristic lines $L\alpha_{2,1}$ and $L\beta_1$ of the copper target at 929.7 and 949.8 eV [121] are reported as well.

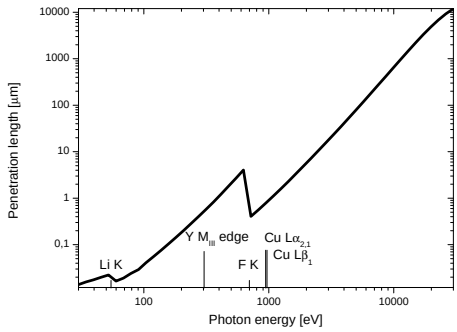

Figure 3.8: Attenuation length of x-rays in LiF [6].

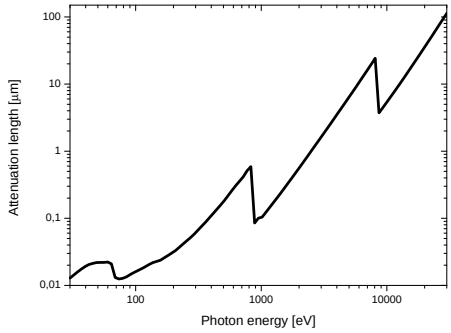

Figure 3.9: Attenuation length of x-rays in nickel [6].

Eleven series of thin films were irradiated at the TVLPS, eight with yttrium and three with copper target. Ten series were exposures in single shot, only the series with the biological samples (parts of a crane fly) was irradiated with 17 shots on the copper target, resulting in an x-ray fluence of 3.72 mJ/cm^2. For spectrophotometer and spectrofluorometer measurements a LiF crystal was included in each series irradiated with single shot of the TVLPS. The first five series each contained two 100 nm thin films on glass substrate, one with a diameter of 18 mm, the other with 10 mm diameter, and one 100 nm film on silicon substrate, one 1 µm film on glass substrate and another 1 µm film on silicon substrate, all of the latter with a diameter of 10 mm. A dragonfly wing was placed on the smaller 100 nm film on glass and the one on silicon, a 4 µm thick 2000lines/inch nickel mesh on the other three LiF thin films for analysis of spatial resolution and contrast. The commercial nickel mesh was chosen due to its well-defined parameters and high x-ray absorption (fig. 3.9); the dragonfly wing, whose x-ray absorption is dependent on composition and thickness, was selected in order to investigate experimental conditions suitable for biological imaging. Three series were irradiated with yttrium (table 3.1), two with copper target (fig. 3.10).

Another series consisted in two LiF films on aluminium, on glass and Si, respectively, and two more LiF films on glass and Si, respectively, all four with a thickness of 160 nm. A series of three 100 nm LiF films each on glass and Si, respectively, was irradiated together. Then we compared three films each, with a thickness of 100 nm and a thickness of 1 µm, one series on glass, the other on Si. Finally, we compared three LiF films grown at 35°C with three grown at 300°C, all with a thickness of 1.4 µm. Unfortunately the LiF films grown at 35° have a lower adhesion and were probably broken even before irradiation like others from the same series. All these LiF thin films were irradiated under vacuum in single shot with yttrium target.

Dr. A. Vincenti measured the thickness of the LiF films used in

Sample				Notes
Substrate	Thickness	Thickness	Dimensions	Partial cover
3.4mJ/cm^2 single shot on yttrium				
bulk	0.5mm		5x5mm	
silicon	155nm	115nm	10mm	dragonfly wing
glass	125nm	120nm	10mm	dragonfly wing
silicon	1,200µm	1,030µm	10mm	nickel mesh
glass	1,155µm	1,040µm	10mm	nickel mesh
glass	137nm	111nm	18mm	nickel mesh
single shot on yttrium				
bulk	0.5mm		5x5mm	
silicon	105nm	135nm	10mm	dragonfly wing
glass	130nm	110nm	10mm	dragonfly wing
silicon	1,025µm	1,170µm	10mm	nickel mesh
glass	1,005µm	1,030µm	10mm	nickel mesh
glass	100nm		18mm	nickel mesh
4.9mJ/cm^2 single shot on yttrium				
bulk	0.5mm		5x5mm	
silicon	80nm	105nm	10mm	dragonfly wing
glass	105nm	90nm	10mm	dragonfly wing
silicon	0,995µm	1,040µm	10mm	nickel mesh
glass	1,065µm	1,105µm	10mm	nickel mesh
glass	100nm		18mm	nickel mesh

Table 3.1: Table of LiF samples irradiated at the University Tor Vergata.

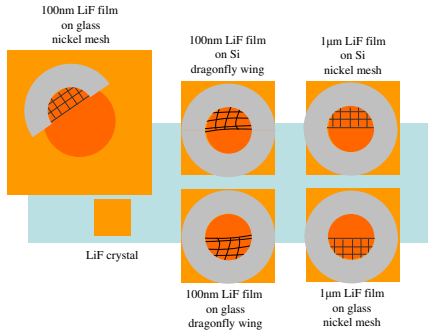

Figure 3.10: LiF samples as prepared for soft x-ray irradiation at the TVLPS.

the irradiations at the TVLPS (table 3.1). Two independent measurements were performed on each LiF film.

3.3 Optical Measurements

3.3.1 Optical Absorption

Measurements of optical absorption were performed both on the samples irradiated at the synchroton source ANKA and those irradiated at the TVLPS. In the latter case, a LiF crystal was included in every series of thin films irradiated with a single shot of the TVLPS. Optical absorption measurements on thin films are rendered difficult by the interference fringes from multiple internal reflections. These measurements are essential since O.D. is proportional to CC density and thus allows to verify the formation of stable defects as well as an estimation of their concentration.

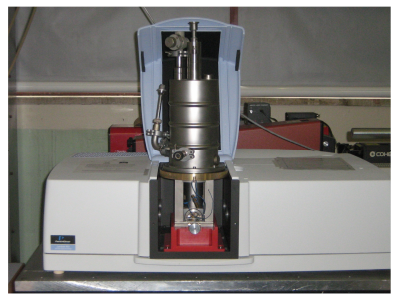

Figure 3.11: PerkinElmer Lambda 950 UV/Vis/NIR spectrophotometer at the ENEA C.R. Frascati.

The PerkinElmer Lambda 950 UV/Vis/NIR spectrophotometer (fig. 3.11) is equipped with a deuterium lamp for the ultraviolet (UV) and a tungsten-halogen lamp for the visible (Vis) and near infrared (NIR) spectral interval. A 1440lines/mm holographic grating selects a segment of the spectrum which becomes near-monochromatic after passing the entrance slit to a second monochromator. The high spectral purity beam from the second monochromator is then split by a chopper with a mirror, a window and two dark segments into signal and reference beam. The dark segments allow for synchronous background control via dark signal acquisition. The transmitted radiation is detected by an R6872 photomultiplier in the visible and UV spectral region and a Peltier cooled lead sulfide (PbS) detector in the NIR.

At the M absorption peak at 450 nm, the O.D. of the uncoloured samples showed a standard deviation of about 3%. The thickness of three samples was measured and found to vary between 0.5 and 0.54 mm. To estimate the inclination of the crystal faces the thickness was measured on opposite sides of the sample, resulting accurate within 0.01 mm. Variations of the transmittance measurements result in-

dipendent of this error. Another possible source of variations between different measurements is the quality of the crystal surfaces which depends on the polishing procedure.

At the beginning of each series of measurements the spectrophotometer lamps need a warm up time of 10-15 minutes before baseline acquisition with sample masks in place. We chose 3 mm diameter masks for the LiF crystals irradiated at the synchroton source ANKA in order to guarantee complete covering of the uncoloured zones due to the sample holder at the margins of the samples and 4 mm masks for the samples irradiated at the TVLPS. The sample is attached to the mask by two strips of biadhesive left and right from the hole where the beam passes, with the irradiated face pointing away from the incoming beam. The scan range is between 1400 and 190 nm. The slit width in the visible and UV spectral regions is fixed to 2 nm, the cycle time is 1 s and the data interval 1 nm. In servo slit mode the slit width is adjusted automatically to obtain constant energy on the detector. This mode is active in the NIR region.

The baseline-corrected O.D. of coloured and uncoloured samples was calculated according to the well-known formula $O.D. = \log(100/T)$ with T the transmittance in percent. The O.D. of the uncoloured samples was substracted to account for attenuation not originating from mechanisms related to CC formation (reflection at the interfaces, Rayleigh scattering and absorption). The offset was corrected at 800 nm and the wavelength transformed in photon energy according to $E[eV] = 1239/\lambda[nm]$. Due to saturation of the instrumental response at an O.D. of about 4 the O.D. at the absorption peak of the F band has to be obtained by interpolation. Though phonon interactions define the broad CC absorption and emission bands [87, 88] a Gaussian interpolation of the F absorption band yields better results than a Lorentzian [122]. Deconvolution of superposed absorption bands, e.g. F_2 and F_3^+ absorption which superimpose to form the M absorption

band, is achieved by interpolation with superimposed Gaussians:

$$y = \frac{A_1}{w_1\sqrt{\pi/2}}\exp(-2\frac{(x-x_{c1})^2}{w_1^2}) + \frac{A_2}{w_2\sqrt{\pi/2}}\exp(-2\frac{(x-x_{c2})^2}{w_2^2}). \quad (3.4)$$

The interpolation yields are the areas of the two Gaussians A_1 and A_2, their waists w_1 and w_2 and their centre positions x_{c1} and x_{c2}.

Assuming a uniform colouration along the crystal thickness, the absorption coefficient is calculated according to $\alpha = 2.3A/d$, where 2.3 is a factor originating from converting $\log_{10}$ to $\log_e$, A the O.D. maximum and d the colouration depth. Simulations of the deposited energy density by Dr. E. Nichelatti yielded a colouration depth of 500µm. The centre density N for a Gaussian absorption band is then calculated according to the Dexter modification of the Smakula formula [8, 123]:

$$N[cm^{-3}] = 0.87 \cdot 10^{17} \cdot \frac{n}{n^2+2}\frac{W[eV]}{f} \cdot \alpha[cm^{-1}]. \quad (3.5)$$

Here n is the refractive index, 1.4203 at 245 nm and 1.396 at 445 nm [48], and W the FWHM of the absorption band. The oscillator strength f is estimated 0.28 for F_2 and F_3^+ centres [52, 124] and 0.56 for F centres [69, 125], and α is the absorption coefficient.

3.3.2 Photoluminescence

The modular spectrofluorometer set-up consists of Coherent Innova I308C cw argon laser at 457.9 nm, Thorlabs MC1F10 optical chopper, HORIBA Jobin Yvon TRIAX 320 monochromator, Hamamatsu H7422-20 photomultiplier and a Stanford Research Systems SR850 DSP lock-in amplifier (fig. 3.12). Each sample was attached to a fixed

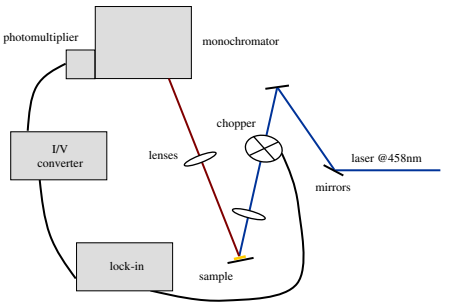

Figure 3.12: Modular spectrofluorometer for PL measurements by lock-in technique.

mount with biadhesive. The different thicknesses of samples and substrates introduce a systematic error, which however was considered preferible to a non-reproducible realignment for every sample. This problem may be solved by a mount allowing for different dimensions while keeping the sample surface in the same position. The laser is polarized vertically and impinges on the sample at an angle of 40° from the sample surface. The fluorescence signal is focused on the monochromator entrance by a 7 cm diameter 8 cm focal length lens (NA=0.44) in the direction perpendicular to the sample surface. A 1200 lines/mm grating blazed for 500 nm was used for the measurements. The TRIAX 320 monochromator reaches a dispersion of 2.64 nm/mm and a resolution of 0.06 nm with an entrance aperture ratio f/4.1 (NA=0.12). Measurements were performed in a spectral interval from 480 to 800 nm in steps of 2 nm with a time constant of 300 ms. The acquired spectra were corrected taking into account the photomultiplier response.

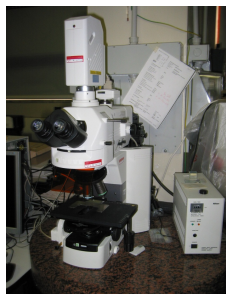

Figure 3.13: Nikon Eclipse 80i-C1 microscope at the ENEA C.R. Frascati.

3.3.3 Confocal Laser Scanning Microscope

The CLSM is utilized as instrument for optical read-out of LiF x-ray imaging detectors. It consists in an optical microscope Nikon Eclipse 80i-C1 (fig. 3.13 which is able to operate in fluorescence mode both in wide field and confocal configuration. Fig. 3.14 illustrates the advantage of a confocal microscope with respect to a conventional one. In the image plane of the objective there is a micrometric pinhole. The name "confocal" derives from the fact that the pinhole is in a plane conjugate to the focal plane of the objective [126]. This pinhole suppresses stray light and light from out-of-focus planes of the sample yielding a smaller point spread function (image space intensity distribution). Due to pointwise excitation with a focused laser beam and pointwise detection the resolution increases by about 30% [127, 128].

Fig. 3.15 is a diagram of the confocal head of the CLSM. The laser pump enters the confocal head via single-mode fibre (1). It is collimated (2) and illuminates the scanning mirrors (4) after reflection on a dichroic mirror (3). It is then focused on the sample by the scanning lens (5). The fluorescence light is collected by lens (6) and

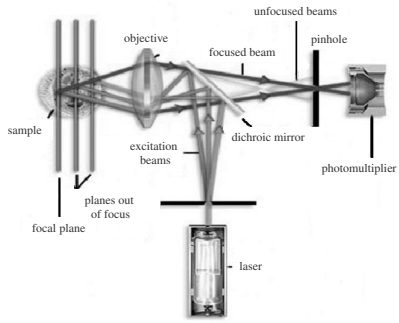

Figure 3.14: Scheme of CLSM with micrometric pinhole [7].

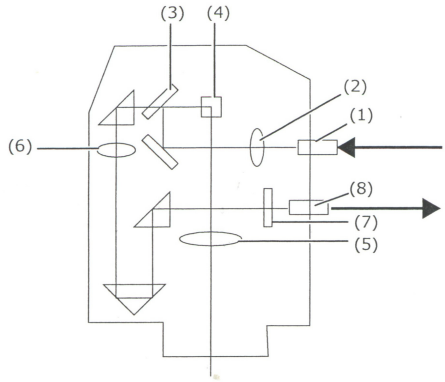

Figure 3.15: Diagram of the confocal head of the CLSM [7].

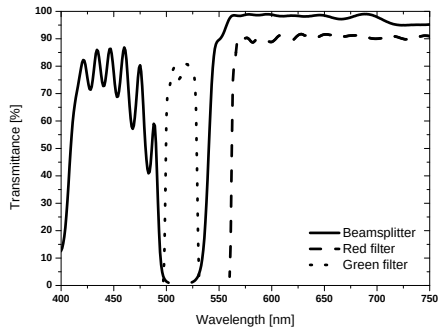

Figure 3.16: Transmittance spectra of red and green filters of the CLSM PMT block as well as beam splitter [7].

reaches the PMT via multimode fibre (8) after passing a pinhole (7).

In fluorescence wide field mode, the PL signal from about 515 nm upwards is collected by the CCD while the sample is illuminated with a properly filtered mercury lamp [7]. The image is then split into the RGB colour channels which are analysed separately. For image acquisition in confocal mode the microscope is equipped with a cw Coherent INNOVA 90 argon laser for CC excitation at 457.9 nm. The PL signal is detected by a system of two Hamamatsu R928 photomultipliers, which acquire separately and independently two different spectral regions selected by appropriate filters. One filter with a bandpass from 560 nm upwards is reserved for detection of the broad F_2 centre emission band peak at 678 nm, the other, with a bandpass between c 495 and 530 nm, for the broad F_3^+ fluorescence band peaked at 541 nm ([7], fig. 3.16). The small spectral interval for the acquisition of F_3^+ centre PL and the lower transmittance of about 80% with respect to c 90% for F_2 centre PL necessitate a higher gain for the green channel.

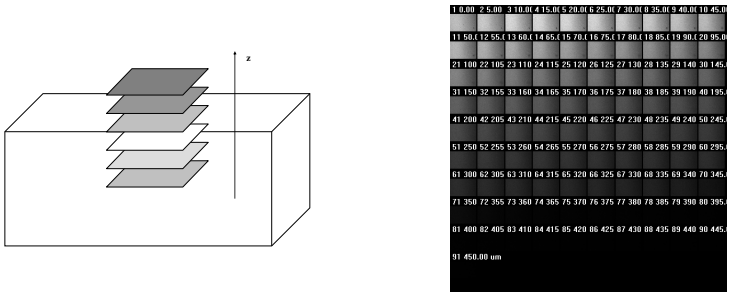

(a) (b)

Figure 3.17: A z-scan consists in a sequence of images of the x-y plane entering along z into the volume of the sample a), z-scan on the LiF crystal irradiated at the synchroton source ANKA for 30 s b).

3.3.4 Colour Centre Distribution

The z-scan was investigated as a direct technique to determine CC distribution. Since in confocal microscopy, the light coming from outside the focal plane is suppressed, the CLSM is an inherently depth-discriminating optical system [129]. The z-scan technique permits optical sectioning of the sample in the vertical direction and successive 3D reconstruction. A z-scan consists in a sequence of fluorescence images of the x-y plane entering along z into the volume of the sample (fig. 3.17). Images of the intensity profile along cleaved lateral surfaces were taken for comparison.

Simulations of the deposited energy density were performed by Dr. E. Nichelatti at the ENEA C.R. Casaccia according to the following model [130]. An x-ray photon of energy E is absorbed at a depth $z + dz$ with the probability:

$$p(E, z)dz = \alpha(E) \exp\big(-\alpha(E)z\big)dz, \tag{3.6}$$

with α the absorption coefficient. The spectral intensity is given by:

$$I(E) = \Phi(E)E, \tag{3.7}$$

with the photon flux Φ. The deposited energy density is defined as:

$$\dot{\rho}_E(z) = \int_0^\infty p(E,z)I(E)dE. \tag{3.8}$$

The deposited energy density was normalized to the total intensity of the x-ray beam:

$$I_{TOT} = \int_0^\infty I(E)dE. \tag{3.9}$$

Colouration and PL are assumed to be proportional to the deposited energy density. A possible threshold and saturation phenomena are neglected on the basis of the experimental results.

3.3.5 Spatial Resolution, Optical Response and Contrast

The intrinsic resolution of the LiF detectors is related to the dimension and diffusion of the CC, i.e. in the order of tens of nanometers.

The lateral spatial resolution r_{xy} and the axial spatial resolution r_z of the CLSM under ideal imaging conditions are defined by [127]:

$$r_{xy} \approx \frac{0.4\lambda_{em}}{NA} \tag{3.10}$$

and

$$r_z \approx \frac{1.4\lambda_{em}n}{NA^2}. \tag{3.11}$$

Here λ_{em} is the emission wavelength and n the refractive index of the specimen. For the 40x objective with a NA of 0.6 we obtain

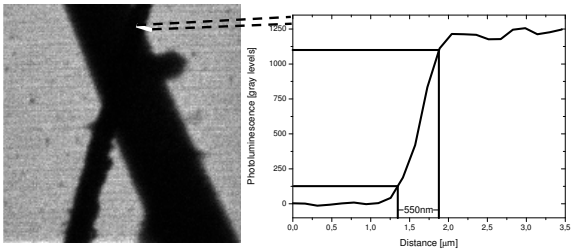

Figure 3.18: Edge resolution in F_3^+ centre PL on 100 nm LiF thin film on glass irradiated at the TVLPS with yttrium target. The fluorescence image was detected by the CLSM system.

lateral resolutions of 361 and 452 nm for F_3^+ and F_2 centre emission, respectively. Pixel size was chosen according to the Nyquist theorem [7].

Soft x-ray contact microradiographies on LiF films exposed at the TVLPS were realized and investigated in terms of spatial resolution, optical response and contrast. The LiF films were covered either with a 4 µm thick 2000lines/inch nickel mesh chosen for its well-defined parameters and high x-ray absorption (see subsection 3.2.2), or with parts of a dragonfly wing, whose x-ray absorption is dependent on its composition and thickness, in order to investigate experimental conditions suitable for biological imaging.

For analysis of spatial resolution we plotted the edge profile of the PL signal detected by the CLSM along a line in a completely x-ray

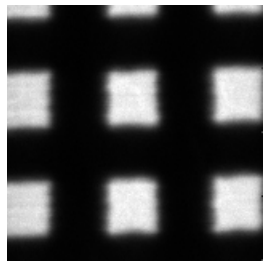

Figure 3.19: F_2 centre PL image of the microradiography of the nickel mesh on a 1 μm LiF film on Si substrate.

exposed (bright area) and covered part (dark area) of the samples as shown in fig. 3.18. Edge resolution is defined as the distance between 10 and 90% of $I_{max} - I_{min}$, with I_{max} and I_{min} the PL intensities of exposed and covered parts of the LiF detectors, respectively. Fig. 3.19 shows the F_2 centre PL image of the nickel mesh microradiography on a 1 μm LiF film on Si substrate

Spatial resolution of the hard x-ray microradiographies on the LiF thin film and crystal irradiated at the synchroton source ANKA was analysed. An Xradia test pattern consisting in a gold mask on a (500x500) μm Si_3N_4 window was exposed at a distance of 17.5 cm from the samples. Fig. 3.20 shows the F_2 centre PL image (detected by the CLSM) of the microradiographies of the Xradia test pattern exposed for 30 s, on a LiF crystal a) and on a 1 μm LiF film on glass substrate b).

We analysed the optical response of soft x-ray microradiographies on LiF films irradiated at the TVLPS as function of substrate and film thickness. We defined optical response as $I_{max} - I_{min}$, the contrast as $(I_{max} - I_{min})/(I_{max} + I_{min})$. The contrast was controlled to make sure

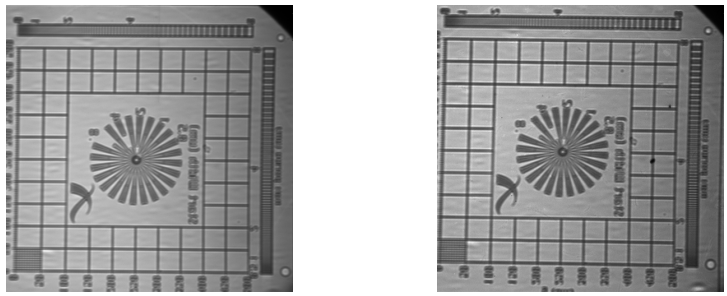

(a) (b)

Figure 3.20: F_2 center PL images (detected by the CLSM) of the microradiographies of the Xradia test pattern exposed for 30 s at the synchroton source ANKA, on a LiF crystal a) and on a 1 µm LiF film on glass substrate b).

there were no negative side effects due to an increased response. Due to the biological nature of the dragonfly wing and the according variations in composition, thickness and in consequence x-ray attenuation these elaborations may meet with small inaccuracies on the LiF thin films covered by parts of the wing. Therefore resolution and contrast of these samples were analysed separately.

3.3.6 Data Interpolation

Absorption and PL spectra are interpolated with Gaussian curves to separate F_2 and F_3^+ centre contributions. The resulting data are plotted as function of irradiation time and interpolated as well to obtain the detector response function. In both cases we need to quantify the

gof. Gof is commonly evaluated by two parameters[131]:

$$reduced\,\chi^2 = \sum_{i=1}^{n} \frac{(y_i - \hat{y}_i)^2}{dof} \tag{3.12}$$

and

$$\bar{R}^2 = 1 - \frac{reduced\,\chi^2}{\frac{TSS}{n-1}}. \tag{3.13}$$

Here y_i are the experimental data, $\hat{y}_i$ are the corresponding values of the interpolating curve and $dof = n - k$, with n the number of data points and k the number of variables. The total sum of squares TSS is given by $\sum_{i=1}^{n}(y_i - \bar{y})^2$ with $\bar{y}$ the mean of the experimental data. The $reduced\,\chi^2$ describes the deviation of the interpolation from the experimental data, i.e. the part of the deviation of the data from their mean which is not explained by the interpolation, while $\bar{R}^2$ gives this deviation in relation to the total variation of the experimental data around the mean value, normalizing it to values between 0 and 1 [131].

The error of the interpolation parameters derives from χ^2 minimization [131]. The partial derivatives with respect to each parameter are set to zero to minimize the derivation between theoretical curve and measured data:

$$\frac{\partial \chi^2}{\partial \theta_j} = -2 \sum_{i=1}^{n} \left(y_i - f(\vec{x}, \hat{\vec{\theta}})\big|_{x_i}\right) \frac{\left(\partial f(\vec{x}, \hat{\vec{\theta}})\big|_{x_i}\right)}{\partial \theta_j} = 0. \tag{3.14}$$

Here θ_j are the fitting parameters, y_i the data points and $f(\vec{x}, \hat{\vec{\theta}})\big|_{x_i}$ the interpolation curve as function of $\vec{x}$ and the fitted parameters $\hat{\vec{\theta}}$ at the point x_i. From the partial derivatives matrix:

$$F_{ij} = \frac{\left(\partial f(\vec{x}, \hat{\vec{\theta}})\big|_{x_i}\right)}{\partial \theta_j} \tag{3.15}$$

we obtain the variance-covariance matrix:

$$\mathbf{C} = (\hat{\mathbf{F}}'\hat{\mathbf{F}})^{-1} \cdot reduced\,\chi^2. \tag{3.16}$$

The error of the parameters is given by:

$$s_{\theta_i} = \sqrt{\hat{C}_{ii}}. \tag{3.17}$$

The main diagonal values of $\hat{\mathbf{C}}$ consist in the sum of squares of partial derivatives in all data points, i.e. they give an estimation of how close to zero the partial derivative and therefore how close to the optimum value the parameter is. These are compared with the mean residual variance χ^2, i.e. how close the interpolation curve is to the experimental data. The sum of partial derivatives in all data points should be larger than the mean residual variance in one data point, and the error calculated this way should be smaller than the value of the parameter.

3.3.7 Semiquantitative Image Analysis

In addition to the visualization of small details, e.g. of insect members, or internal structures such as blood circulation or cell organelles [34, 5], it is also possible to obtain quantitative information from x-ray contact microscopy. Quantitative analysis has important applications in Life Sciences, for example to explain calcification, protein and metal accumulation processes or exudate production in tissue sections or cell cultures [1, 132, 5].

We estimated the thickness of a crane fly wing by analysis of the fluorescence intensity profiles of its x-ray microradiography on a LiF detector. We assume that the diameter of a thin rib measured on the x-ray microradiography corresponds to the material thickness in the orthogonal direction. Taking into account the x-ray absorption in this part of the image we are able to calculate the thickness of the organic

material in any other part of the image [5] assuming that the material remains the same.

The x-ray dose D_r on the detector surface under the rib is given by:

$$D_r = D_{r0} exp(-\beta x_r), \tag{3.18}$$

with D_{r0} the x-ray dose impinging on the rib, β the x-ray absorption coefficient and x_r the thickness of the rib. The x-ray dose D_i on any other part of the wing is given by:

$$D_i = D_{i0} exp(-\beta x_i), \tag{3.19}$$

with the impinging x-ray dose D_{i0} and the thickness of organic material x_i. For soft x-rays the colour centre density and thus the intensity E of the fluorescence image is proportional to $D^{0.5}$ [12]. From equations 3.18 and 3.19 we obtain:

$$x_i = x_r \frac{ln(E_i^2/E_{i0}^2)}{ln(E_r^2/E_{r0}^2)}. \tag{3.20}$$

Here E_i is the fluorescence intensity in the part of the detector where the thickness of the absorbing material is to determine, E_{i0} the fluorescence intensity due to the impinging x-ray dose in proximity of this point, E_r the fluorescence intensity in the area covered by the rib and E_{r0} the fluorescence intensity due to the impinging x-ray dose in proximity of the rib.

Chapter 4

LiF Imaging Detectors: Results

4.1 Introduction

In this chapter we present a comprehensive analysis of the optical response of the LiF x-ray imaging detector. We investigated the detector response function in absorption and PL as well as resolution and contrast. An example for semiquantitative image analysis is presented as well. The chapter is divided into two sections regarding the irradiations at the synchroton source ANKA (section 4.2) and at the TVLPS (section 4.3).

4.2 Synchroton Source Irradiation

4.2.1 Absorption and Defect Density

Transmittance measurements on the five LiF crystals uniformly irradiated at the TopoTomo beamline of the synchroton source ANKA (see

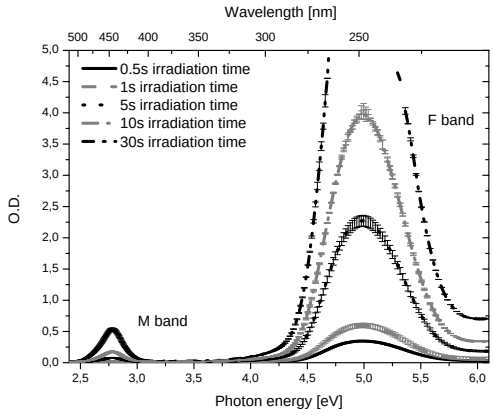

Figure 4.1: RT absorption spectra for five LiF crystals x-ray irradiated at the synchroton source ANKA with exposure times from 0.5 to 30 s.

subsection 3.2.1) were performed at RT with a PerkinElmer Lambda 950 UV/Vis/NIR spectrophotometre described in subsection 3.3.1. Fig. 4.1 shows the absorption spectra of the five LiF crystals irradiated with exposure times from 0.5 to 30 s. Formation of stable primary defects is demonstrated by the presence of the F absorption band, while F_2 and F_3^+ centre absorption superimpose in the M absorption band.

Interpolation was performed in the spectral interval of the absorption band, between 4.3 and 5.7 eV for the F band and from 2.55 to 3 eV for the M band. Since a deconvolution of the M absorption band was impossible for irradiation times of 0.5 and 1 s, the M band was interpolated with a single Gauss function for these two samples and attributed to absorption of the F_3^+ majority defects. Fig. 4.2 shows the F a) and M bands b) with the Gaussian interpolation. The experimental data are black lines and the cumulative interpolation is represented by corresponding gray lines, while the F_2 and F_3^+ absorption bands, respectively, are fitted with a solid and a dashed gray line.

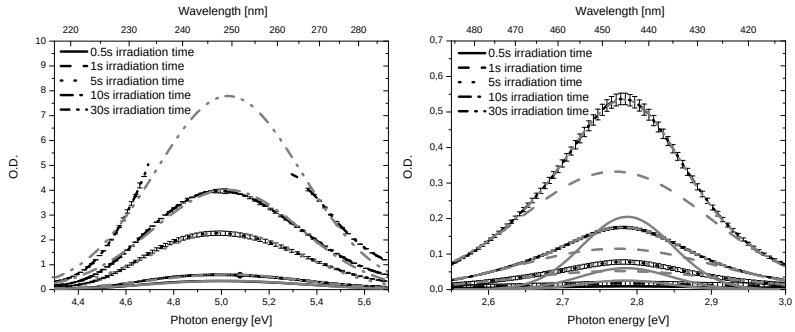

(a) (b)

Figure 4.2: Gaussian interpolation of the F band a) and deconvolution of the M band b) for the five LiF crystals irradiated at the synchroton source.

Irradiation time [s]	*reduced* χ^2 [a.u.]	$\bar{R}^2$ [ ]
0.5	1.69E-4	0.98476
1	5.28E-4	0.98433
5	7.51E-3	0.98554
10	1.96E-2	0.98743
30	1.13E-1	0.93415

Table 4.1: Gof for the Gaussian interpolation of F centre absorption.

Irradiation time [s]	A [a.u.]	FWHM [eV]	x_c [eV]
0.5	0.286 ± 2.56E-3	0.759 ± 8.22E-3	5.022 ± 3.24E-3
1	0.495 ± 4.52E-3	0.766 ± 8.43E-3	5.023 ± 3.34E-3
5	1.83 ± 1.66E-2	0.741 ± 8.07E-3	5.019 ± 3.23E-3
10	3.13 ± 2.66E-2	0.734 ± 7.43E-3	5.023 ± 2.99E-3
30	5.9 ± 1.47E-1	0.75 ± 2.02E-2	5.029 ± 5.11E-3

Table 4.2: Parameters of the Gaussian interpolation of the RT F absorption band in LiF crystals irradiated at the synchroton source Anka.

Tables 4.1 and 4.2 show gof as well as the parameters of the F absorption band resulting from interpolation. These parameters are in good aggreement with the literature (table 4.3). The interpolation procedure depends on the included data points and is precise only up to two decimal points even if the errors of the parameters are smaller. The errors of the interpolation for the F absorption band of the crystal irradiated for 30s in particular are larger than those from interpolation of the existing data listed in the table due to the missing data points.

Fig. 4.3 shows the O.D. of the F centre absorption band as function of irradiation time. Saturation for higher irradiation times is clearly distinguished. The detector response function depends not only on the spectral interval of the x-ray source, but on other irradiation parameters such as dose rate and irradiation temperature [74], as well as material properties, e.g. the presence of impurities (see subsection 2.4.2). Thus there are large variations in the dependence of O.D., centre density and PL on the x-ray dose and dose rate reported in the

Absorption band	x_c [eV]	x_c [nm]	FWHM [eV]	$\alpha[cm^{-1}]$	References
F	5.12	242	-	-	[77, 133]
F	4.96	250	-	-	[77, 134]
F	4.96	250	-	-	[77, 135]
F	4.96	250	-	-	[77, 136]
F	5.10	243	-	-	[77, 137]
F	4.96	250	-	68.7-121	[77, 138]
M	2.76	450	-	5-10	[77, 138]
F	4.96	250	-	170-450	[77, 138]
M	2.76	450	-	17-75	[77, 138]
F	4.96	250	-	30-100	[77, 139]
M	2.76	450	-	2-8	[77, 139]
F	5.00	248	0.76	-	[140]

Table 4.3: Peak position and FWHM of the RT F and M absorption bands in LiF as reported in the literature.

literature.

For soft x-rays at about 0.05-2 keV from a laser plasma source with yttrium target the LiF thin film (1μm, glass substrate) response in PL as function of the x-ray dose D was found to be proportional to $D^{0.35}$ for F_3^+ and $D^{0.45}$ for F_2 centres [141]. A copper target yielded exponents of 0.45 and 0.8, respectively [141]. Another laser plasma source emitting between 0.02 and 1.5 keV gave rise to a response proportional to $D^{0.5}$ for both types of aggregate defects in absorption, centre density and PL [12]. The centre densities achieved in LiF crystals with a 12 keV electron beam were not interpolated as function of irradiation time, but the increase of F_3^+ centre density is sublinear, while F and F_2 centre density are close to saturation [122]. The PL

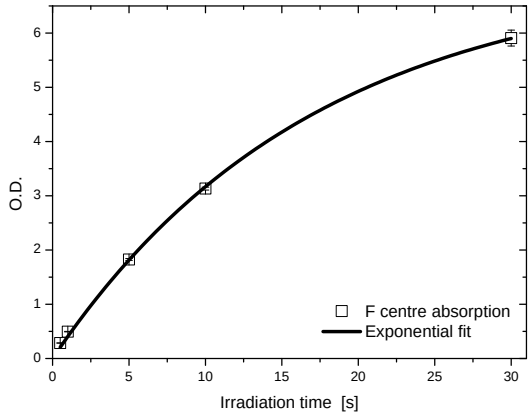

Figure 4.3: Increase in the O.D. of the F absorption band of the five LiF crystals irradiated at the synchroton source ANKA as function of irradiation time and exponential interpolation.

signals from 3 μm thick LiF films on fused silica substrates irradiated with γ-rays increased sublinearly with irradiation dose for both F_2 and F_3^+ centres as well [93]. The increase of the PL signals obtained for colouration of LiF crystals with a laboratory x-ray tube peaked at a photon energy of 8 keV as function of exposure time, on the other hand, is slightly superlinear [142]. In KCl a parabolic increase of F centre density with saturation has been observed [72]. Various experiments provided colouration kinetics in LiF in concordance with the Thévenard model [143, 144, 145, 45], while a dose-like response with saturation was found for colouration of a LiF with ultrashort pulses from a Ti:sapphire CPA laser operating at 830 nm [146], but also for irradiation of a 200 nm LiF thin film on glass substrate with SHI [38].

The increase in centre density is initially linear and saturates at higher doses and thus higher densities of electronic excitation due to increased recombination of vacancies and interstitials as well as for-

mation of more complex aggregate centres [145, 143]. In AH radiation damage takes place preferably in the halogen sublattice [45]. CC density can not become arbitrarily high [69], as large aggregates of halogen vacancies collapse into small Li colloids [45, 8]. Though LiF does not amorphize the material becomes brittle for large defect densities [46].

For irradiation with 3 keV electrons saturation values of CC density have been determined at about $7 \cdot 10^{20}$ F centres/cm^3 and 10^{20} M centres/cm^3 [69]. F centres are close to saturation at $3.3 \cdot 10^{19}$ centres/cm^3 and F_2 centres at $7 \cdot 10^{18}$ centres/cm^3 for irradiation with 12 keV electrons [122]. F centre density was found to saturate at about 10^{19} centres/cm^3 for SHI irradiation with different ions species and energies [145]. F_2 centre concentration was found to saturate at about $5.25 \cdot 10^{20}$ centres/cm^3 under SHI irradiation [38].

The models for colouration kinetics in LiF are described in subsection 2.4.2. According to Farge the saturation follows an exponential law [72], and Thévenard introduced an exponential equation [76]:

$$OD = OD_s(1 - exp(-ct)), \tag{4.1}$$

where t is the irradiation time and OD_s the optical density at saturation. The constant c originally related to the radius of the ion tracks [76] depends on other irradiation parameters and material porperties described by Agulló-López et al. [74]. We obtain an excellent agreement with the values of (7.2±0.20) s^{-1} and 0.059±0.003 for OD_s and c, respectively (fig. 4.3). The centre density at saturation estimated with the Smakula-Dexter formula amounts to $1.1 \cdot 10^{19}$ F centres/cm^3. This value is in good agreement with some of the values reported in literature [122, 145].

Due to the overlap of the F_2 and F_3^+ absorption bands there is a large variation of their parameters reported in the literature [8]. Nonetheless we obtained a good agreement with the values from literature. For synchroton irradiation with x-rays from 6-40 keV there is a preferred formation of F_3^+ centres with respect to F_2 centres. No

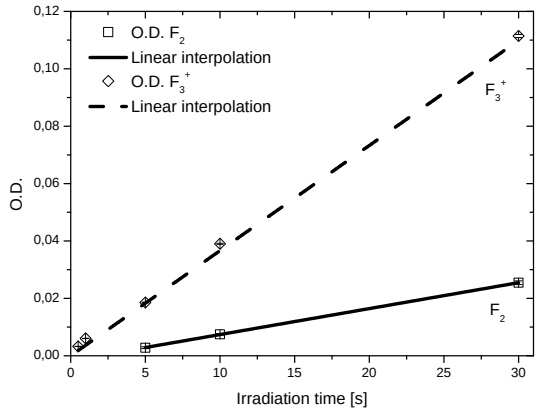

Figure 4.4: Increase in the O.D. of the F_2 and F_3^+ absorption bands of the five LiF crystals irradiated at the synchroton source ANKA as function of irradiation time with linear interpolation.

trend in the variation of peak position and FWHM of the F, F_2 and F_3^+ absorption bands is observed for the five LiF crystals.

Figure 4.4 shows the increase of F_2 and F_3^+ O.D. as function of irradiation time. Their behaviour is linear for both kinds of aggregate defects in the same investigated irradiation conditions. Since the background due to light attenuation from the uncoloured sample has been subtracted, the interpolation is performed with the offset restricted to values smaller than or equal to zero.

The detector response of F_2 and F_3^+ centre absorption can be described by:

$$OD_{F_2} = 9.04 \cdot 10^{-4} s^{-1} \cdot t - 1.64 \cdot 10^{-3} \tag{4.2}$$

and

$$OD_{F_3^+} = 3.66 \cdot 10^{-3} s^{-1} \cdot t, \tag{4.3}$$

respectively, with the irradiation time t measured in s. The negative

Irradiation time [s]	F centre density [cm^{-3}]	F_2 centre density [cm^{-3}]	F_3^+ centre density [cm^{-3}]
0.5	5.4E17±2.0E16	-	4.9E15±2.0E14
1	9.4E17±3.5E16	-	9.1E15±3.7E14
5	3.5E18±1.3E17	1.9E15±2.2E14	2.8E16±1.1E15
10	5.9E18±2.2E17	4.9E15±2.7E14	5.9E16±2.4E15
30	1.1E19±4.9E17	1.7E16±8.5E14	1.7E17±6.7E15

Table 4.4: Centre density of F, F_2 and F_3^+ centres estimated with the Dexter-Smakula formula.

offset is ascribed to instrumental sensitivity, and for F_2 centre absorption corresponds to an irradiation time of 1.8 s.

Table 4.4 shows the centre densities for F, F_2 and F_3^+ centres calculated with the Dexter-Smakula formula.

Fig. 4.5 shows the enlarged absorption spectrum of the LiF crystal irradiated for 5 s at the synchroton source ANKA with the contributions of other aggregate centres (see section 2.4.2). Although the presence of F_3 centres is derived from the R_2 absorption band peaked at 3.31eV/374nm [8], PL contributions of these centres are negligible since their absorption is far from the argon laser excitation at 457.9nm on the low energy side of the M band. The superimposed absorption bands due to other complex aggregate centres amount to less than 5% of the M band peak.

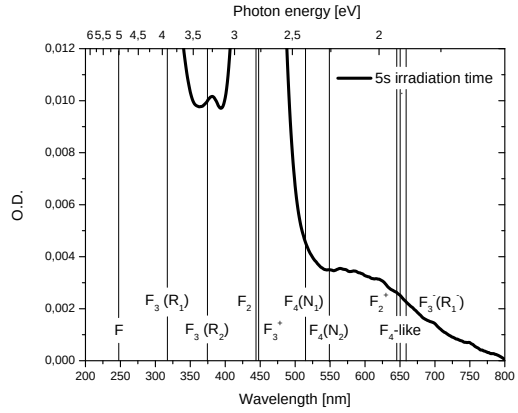

Figure 4.5: RT O.D. of the LiF crystal irradiated for 5s at the synchroton source ANKA with absorption peaks of complex aggregate centres.

4.2.2 PL Detector Response

We acquired laser-excited PL spectra of the five LiF crystals irradiated at the TopoTomo beamline of the synchroton source ANKA (see section 3.2.1) by lock-in technique with the modular spectrofluorometer set-up described in subsection 3.3.2. The partial overlapping of the broad F_2 and F_3^+ emission bands, centred at 678 and 541 nm, respectively [9, 81], implies a deconvolution as the sum of two Gaussian bands according to the literature [81]. Fig. 4.6 shows the RT emission spectra of the LiF crystals irradiated for 0.5, 1, 5, 10 and 30 s at the synchrotron source ANKA, interpolated with Origin software. The squares represent experimental data, F_2 and F_3^+ emission bands are black dashed and dotted lines, respectively, and the solid gray line is the cumulative best fit. All five interpolations are in excellent agreement with the measured PL spectra. FWHM and peak

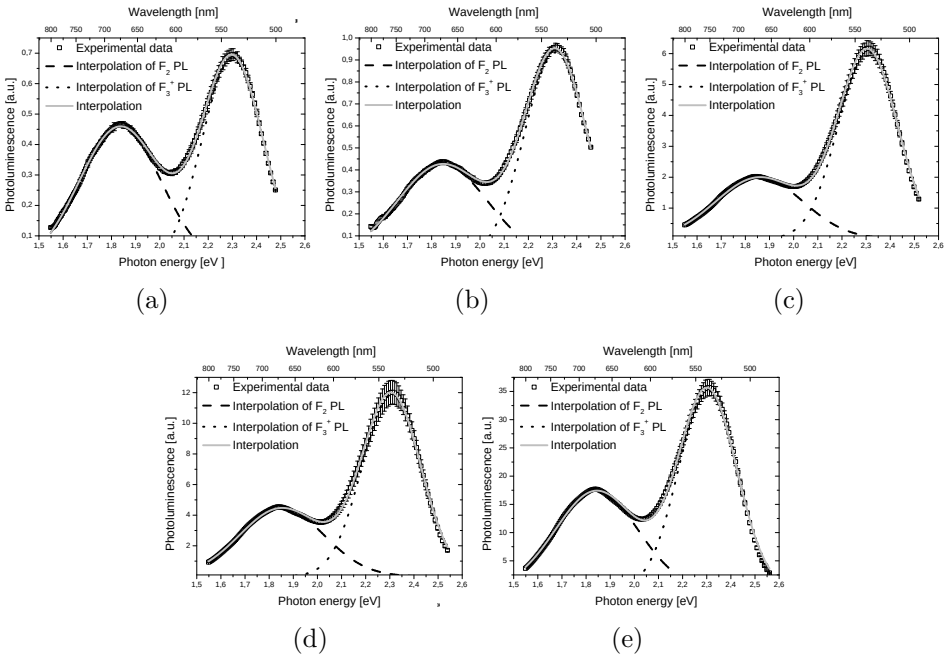

Figure 4.6: Deconvolution of RT PL spectra by interpolation with two superimposed Gaussians for five LiF crystals, x-ray irradiated at the synchroton source ANKA with exposure times of 0.5 s a), 1 s b), 5 s c), 10 s d) and 30 s e).

Absorption band	x_c [eV]	x_c [nm]	FWHM [eV]	References
F_2	1.83	678	0.36	[8, 78]
	1.83	678	0.36	[81]
	1.83	678	0.36	[140]
	1.85	670	0.279	[79]
	1.85	670	0.331	[10]
F_3^+	2.29	541	0.31	[8, 78]
	2.29	541	0.31	[81]
	2.30	539	0.347	[79]
	2.30	539	0.260	[10]
	2.31	536	0.32	[147]

Table 4.5: Parameters of the RT F_2 and F_3^+ emission bands in LiF as reported in the literature.

position obtained by interpolation for the F_2 and F_3^+ centre emission bands are in good agreement with the values reported in the literature (table 4.5).

Fig. 4.7 a) and b) shows a comparison between the LiF crystal detector response functions in absorption and PL for F_2 and F_3^+ centres, respectively. The signals were normalized to the maximum at an irradiation time of 30 s and the linear interpolation was performed with the offset limited to values smaller than or equal to zero. The slopes are (0.0355±2.3E-4) s^{-1} and (0.033±1.6E-3) s^{-1} for F_2 centre O.D. and PL, respectively, while they are (0.0329±8.5E-4) s^{-1} and (0.0333±3.4E-4) s^{-1} for F_3^+ centre O.D. and PL. The response in PL is directly proportional to the absorption for both kinds of aggregate defects.

In addition to the spectroscopy measurements with lock-in tech-

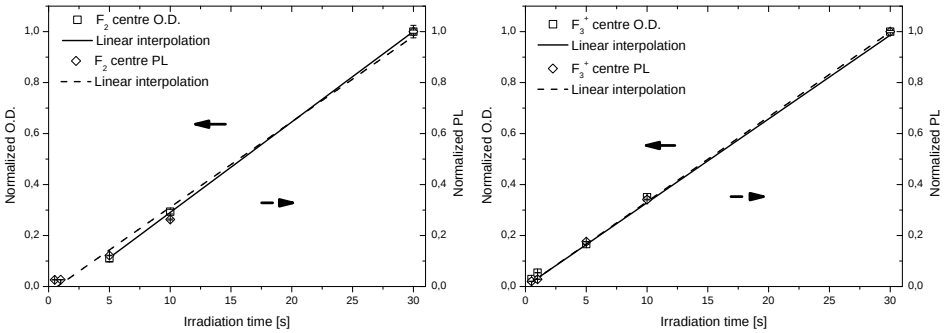

(a) (b)

Figure 4.7: Comparison of LiF crystal detector response (normalized absorption and PL) for a) F_2 and b) F_3^+ centres.

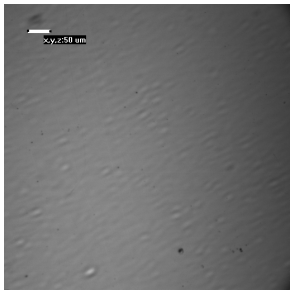

Figure 4.8: Fluorescence surface image of LiF crystal irradiated for 30 s acquired with the CLSM in confocal mode.

nique we performed PL intensity measurements with the CLSM at RT. In order to avoid optical bleaching as well as significant population trapping due to the metastable triplet state involved in the optical cycle of F_3^+ centres the laser pump intensity on the sample was kept as low as possible, i.e. the CLSM fluorescence images of the sample surface (fig. 4.8) were acquired with a 20x objective with NA 0.5. The surface shows scratches originating from the polishing procedure [148]. The maximum pinhole aperture of 150 μm was chosen to maximize the detected PL signal. Measurements in confocal configuration were performed with a pixel size of (1243.2x1243.2) nm and a pixel dwell (integration time on one pixel) of 1.44 μs over an area of (636.5x636.5) μm. The resulting image is composed of (512x512) pixels and averaged over 10 scans. We started with PMT gains of 3.95 and 3.25 for the green and red channels, respectively, in confocal configuration and an exposure time of 1/250 s in wide field configuration. Surface images of the samples irradiated for 30, 10 and 5 s were aquired with these values, then we had to increase gains and exposure time, respectively, to 5.1, 4.45 and 1/30 s for the less irradiated samples. The two acquisitions for the sample irradiated for 5 s yielded a coefficient to scale the PL intensity of the fluorescence images acquired with higher gains. This behaviour demonstrates that in the investigated irradiation conditions the LiF detector has a dynamic range larger than the 12 bit corresponding to the dynamic range of the CLSM image acquisition software.

Fig. 4.9 is a comparison between the increase of F_2 a) and F_3^+ centre b) PL intensities as function of irradiation time from the interpolation of the spectroscopy measurements with lock-in technique and PL measurements with the CLSM for F_2 and F_3^+ centres, both in wide field and confocal configuration. The data were normalized to the maximum PL for an irradiation time of 30 s. The linear interpolation was performed with the offset restricted to values smaller than or equal to zero since there is no PL from uncoloured samples.

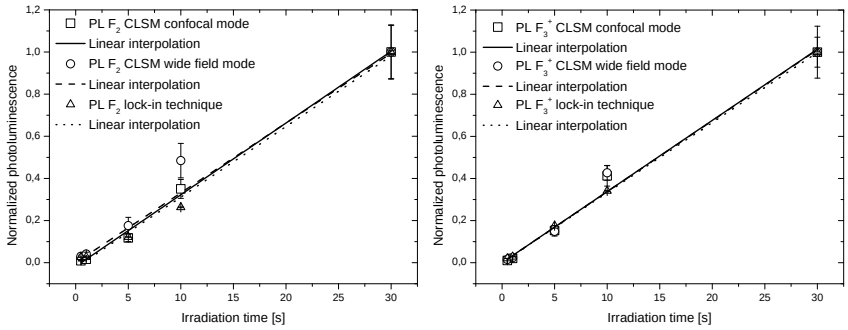

(a) (b)

Figure 4.9: F_2 a) and F_3^+ centre PL signal b) in x-ray irradiated crystals as function of irradiation time, normalized at the maximum exposure time of 30 s.

In conclusion, for photon energies between 6 and 40 keV (ANKA synchroton) the PL increase is proportional to the increase in absorption for the investigated dose interval, i.e. there is no deviation from the linear response function due to the influence of other mechanisms dependent on irradiation time, e.g. concentration quenching. Moreover, the normalized results display the same slope, i.e. the same response function. This proves the reliability of the CLSM as read-out instrument and the robustness of the PL signal. In addition, while F_2 centre absorption is not detectable in the two samples irradiated for 0.5 and 1 s, a detector working in PL is more sensitive and able to detect even weak signals.

The PL response of x-ray irradiated LiF films was also investigated. A comparison between the PL signal of a bulk LiF crystal and a 1 μm thick LiF thin film on glass substrate as well as its trend as function of irradiation time was performed employing the two corresponding sam-

ples with microradiographies of Xradia test patterns irradiated with exposure times between 1 and 30 s. Fluorescence images of the microradiographies were acquired with the CLSM in confocal configuration, employing a 20x objective with a NA of 0.5 and a pinhole aperture of 150 μm. The (636.5x636.5) μm image was composed of (512x512) pixels with a pixel size of (1243.2x1243.2) nm and a pixel dwell of 6 μs. All images were averaged over 10 scans. For exposure times of 30, 20 and 10 s of the bulk sample we used gains of 2.7 and 2.1 for the green and red channels, respectively, while the microradiographies generated with irradiation times of 10, 5, 2.5, 2 and 1 s were read-out with gains of 3.5 and 2.9. The lower gain with respect to the uniformly coloured crystals (see page 64) is due to the higher pixel dwell. The LiF thin film, on the other hand, was read-out with gains of 4.3 and 3.5 for the green and red channels, respectively, for exposure times between 30 and 10 s, and with 5.1 and 4.3 for irradiation times from 10 to 1 s.

Fig. 4.10 shows the comparison of bulk and thin film PL intensities for F_2 a) and F_3^+ centre PL b). The PL signal from the Xradia test pattern microradiographies on a LiF crystal and thin film displays the same linear trend as a function of irradiation time as already found for the five uniformly coloured crystals. In the analysed experimental conditions (e.g. film thickness, substrate, irradiation parameters) colouration kinetics in LiF crystals and thin films are qualitatively identical.

The detector response functions in F_2 and F_3^+ centre PL, respectively, in the employed experimental conditions, for read-out with the CLSM and normalization at an irradiation time of 30 s, are the following:

$$PL_{F_2} = 0.0337 s^{-1} \cdot t - 0.011 \tag{4.4}$$

and

$$PL_{F_3^+} = 0.0336 s^{-1} \cdot t, \tag{4.5}$$

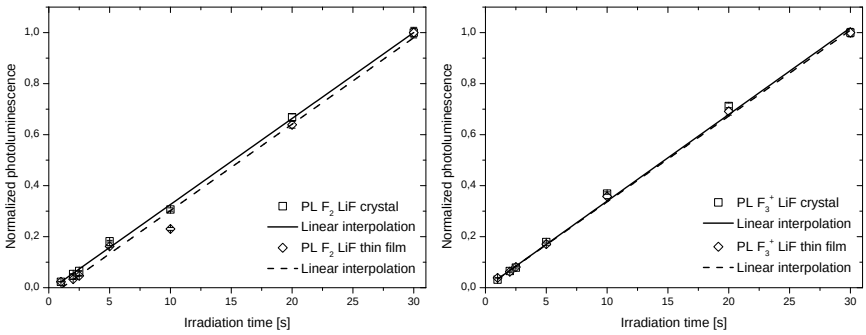

(a) (b)

Figure 4.10: Comparison of F_2 a) and F_3^+ centre PL b) CLSM signal as function of irradiation time for a LiF crystal and a 1µm thick LiF thin film on glass substrate, normalized at the maximum exposure time of 30 s.

with t the irradiation time in s.

4.2.3 Colour Centre Depth Profiles

Due to the large x-ray spectral interval (6-40 keV) covered by the synchroton source ANKA the x-ray beam attenuation lengths vary on a wide interval [6] and the colouration depth in the LiF crystals can not be predicted. The ANKA synchroton source emission maximum is at about 6 keV corresponding to an attenuation length of about 0.3 mm, while the maximum photon energy reaches up to 40 keV with an attenuation length of more than 10 mm [6]. The thickness of 0.5 mm of the LiF crystals is comparable with the attenuation length of 9 keV x-ray photons in this material [6]. In a z-scan a sequence of (x-y) fluorescence images is acquired changing the position along z. We investigated the z-scan with the CLSM for crystals as a direct technique

to determine the CC distribution. In order to study the relationship between PL signal and CC distribution we performed z-scans with the CLSM (λ_{exc}=457.9 nm) starting from both the irradiated front and rear surfaces of the LiF crystals (see 3.17 a). Afterwards one of the LiF crystals was cleaved and we acquired CLSM images of the lateral surface, parallel to the irradiation direction.

The z-scan was performed acquiring (512x512) pixel images of a (636.5x636.5) μm x-y surface, giving a picel size of (1243.2x1243.2) nm. We used a 20x objective with a NA of 0.5 and a pinhole aperture of 150 μm. Both z-scans on the samples irradiated for 0.5 s were performed with gains of 6.5 and 5.8 for the green and red channel, respectively. For the z-scans on the sample irradiated for 30 s we used 3.9 and 3.1, respectively. The samples were analysed over a z-range of 455 μm or 91 steps of 5 μm each, and the images are averages of 5 scans. The step size corresponds to the adjustment of the sample holder position with respect to the objective, i.e. 5 μm in air correspond to an optical path length of 6.95 μm in LiF. The single images of the z-stack are then converted to TIFF format and analysed using the software ImageJ which provides the mean gray scale level and its standard deviation. Fig. 4.11 shows the decay of F_3^+ centre PL as function of distance from the front surface for the five coloured LiF crystals x-ray irradiated with exposure times of 0.5 s, 1 s, 5 s, 10 s and 30 s. The complete decrease of the PL signal at a depth of about 0.5 mm corresponds to the total thickness of the crystal.

Fig. 4.12 shows the F_3^+ centre PL intensity profiles obtained from the z-scans for the LiF crystal irradiated with an exposure time of 30s. For the LiF crystal irradiated for 0.5 s the z-scan PL profiles starting from front and rear surface are nearly identical, while we observe a large difference between the two z-scan PL profiles on the sample irradiated for 30 s. The main mechanisms responsible for the observed behaviour could be the absorption of the laser pump at 457.9 nm by F_2 and F_3^+ defects in each layer and/or reabsorption of the CC

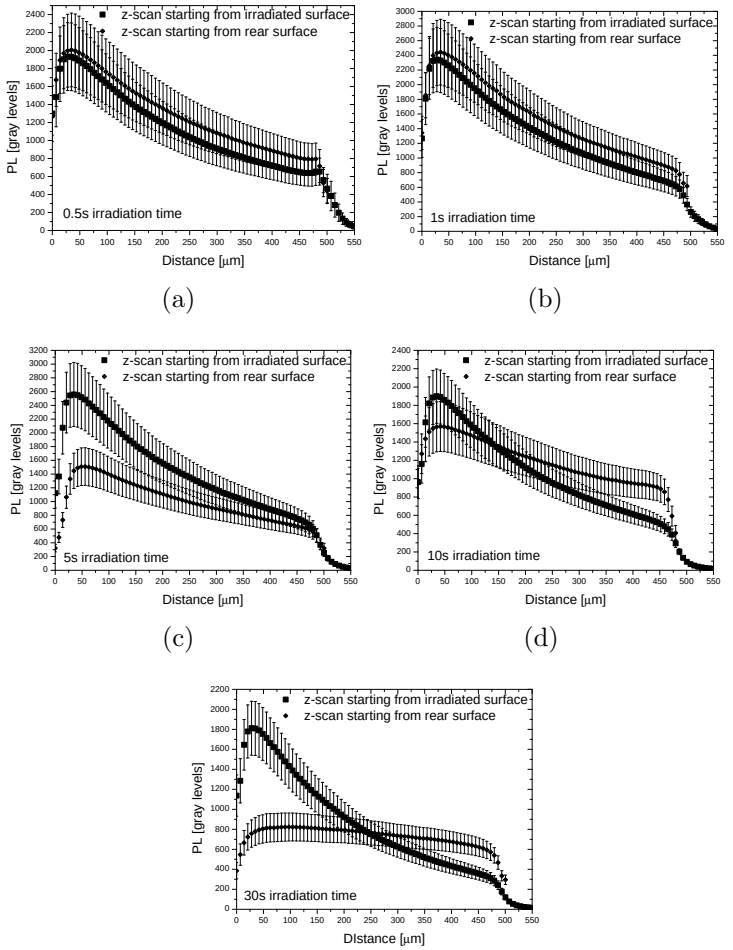

Figure 4.11: CLSM F_3^+ centre PL signals as function of distance from the irradiated surface for LiF crystals coloured at the synchroton source ANKA for a) 0.5 s, b) 1 s, c) 5 s, d) 10 s and e) 30 s for z-scan measurements in front and rear configuration.

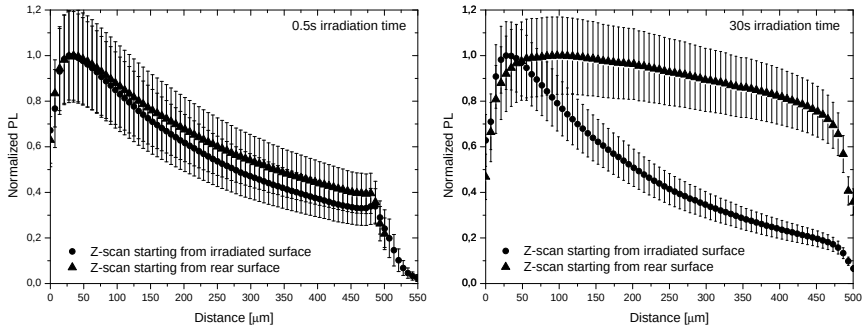

(a) (b)

Figure 4.12: F_3^+ centre PL profiles along the irradiation direction from front and rear z-scans for two LiF crystals irradiated at the synchroton source ANKA with exposure times of a) 0.5 and b) 30 s.

PL due to the large excitation volume. Photobleaching may play a role due to the increased exposure time of the z-scan with respect to single images. In order to investigate some of these aspects the fluorescence image of the lateral surface of the cleaved crystal was acquired with a 4x objective with NA 0.13 to obtain the complete F_3^+ centre PL profile along the irradiation direction and is reported in fig. 4.13. The (x-y) image consists of (720x720) pixel on (0.6x0.6) mm which corresponds to a pixel size of (0.8x0.8) μm. The image was acquired with a pinhole aperture of 30 μm and a pixel dwell of 1.44 μs with gains of 5.9 and 5.2 for the green and red channels, respectively, and averaged over 5 scans.

Fig. 4.14 a) shows a comparison of the deposited energy density simulated by Dr. E. Nichelatti and the lateral PL intensity profile of the sample irradiated for 30 s. The experimental data are restricted to the sample thickness which might explain the deviation in the slopes.

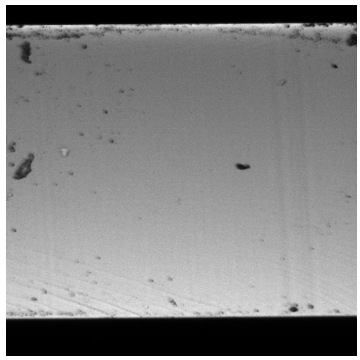

Figure 4.13: CLSM fluorescence image of the cleaved surface of the LiF crystal irradiated for 30s at the synchroton source ANKA. The irradiated surface is on the bottom of the image, the rear surface on the top.

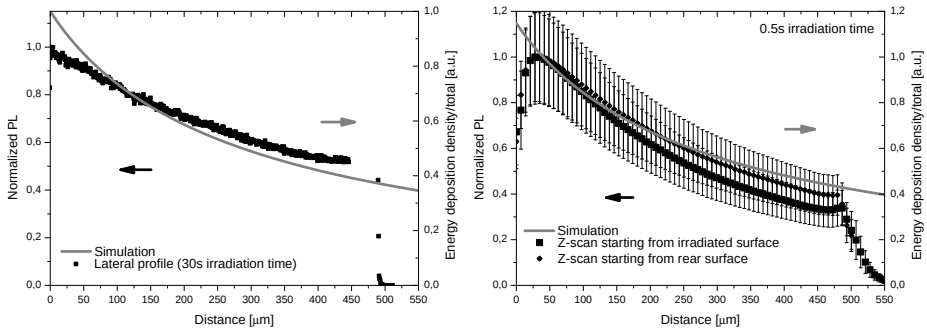

(a) (b)

Figure 4.14: Comparison of the simulated deposited energy density with the lateral PL intensity profile of the sample irradiated for 30 s a) and the z-scans on the sample irradiated for 0.5 s b).

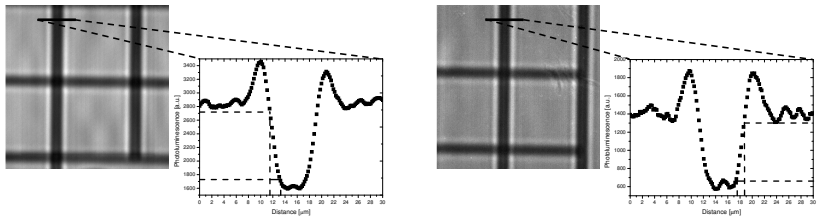

(a) (b)

Figure 4.15: Enlarged microradiographies of Xradia test patterns on LiF crystal a) and 1µm LiF thin film b) and edge profile.

A saturation of CC formation has not been observed for F_2 and F_3^+ centres. Fig. 4.14 b) shows a comparison with the two z-scans performed on the LiF crystal irradiated for 0.5 s. The curves have a similar slope though the slope of the simulated curve with an attenuation length of 500 µm is a bit lower than that of the experimental data. Again, small deviations might be due to the restricted data interval. For samples with low CC concentrations it is possible to estimate CC distribution with the z-scan technique.

4.2.4 X-ray Imaging of Test Patterns

To analyse the spatial resolution PL images of the test pattern microradiographies were acquired using a 40x objective with a NA of 0.6 (see subsection 3.3.5). A pinhole aperture of 150 µm was employed with a pixel dwell of 1.44 µs. (512x512) pixel with a pixel size of (157.9x157.9) nm on an area of (80.8x80.8) µm were used for the green channel and a pixel size of (197.7x197.7) nm on an area of

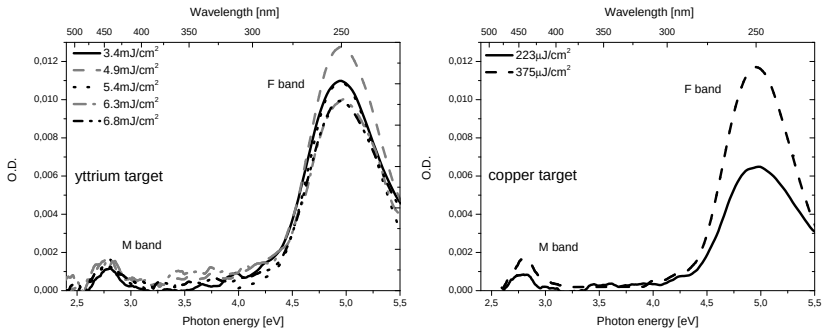

(a) (b)

Figure 4.16: RT absorption spectra of LiF crystals x-ray irradiated at the TVLPS with single shot for a) yttrium and b) copper target.

(101.2x101.2) µm was employed for the red channel.

Fig. 4.15 a) and b) show the enlarged parts of the microradiographies on the crystal and thin film, respectively, with the edge profiles. Diffraction leads to an enhancement of the borders. We obtain a resolution of 1.8 µm for the crystal and of 1.2 µm for the thin film. A higher resolution for the thin film was expected because the colouration and thus the backgroud signal is limited to the film thickness of 1 µm. The contrast of the microradiographies on the LiF crystal and thin film is similar with a value around 0.4.

4.3 Laser-Plasma Source Irradiation

4.3.1 Detector Response in Absorption

Ten commercial LiF crystals were irradiated at the TVLPS in single shot experiments on yttrium and copper targets to study their

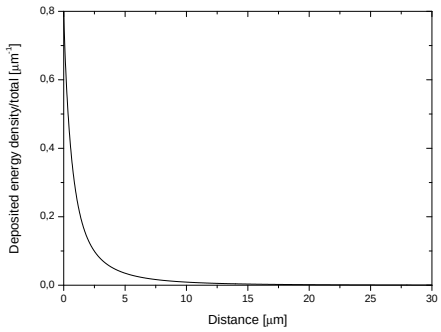

Figure 4.17: Simulation of deposited energy density as function of distance from the surface.

optical response. The Perkin Elmer Lambda 950 UV/VIS/NIR spectrophotometer (subsection 3.3.1) was employed for RT transmittance measurements on the LiF crystals. The transmittance spectra of the LiF crystals were acquired before and after irradiation at the TVLPS (see subsection 3.2.2). The O.D. was calculated as in subsection 4.2.1 and the offset corrected on both sides of the M band after subtraction of the attenuation obtained for the uncoloured sample. Fig. 4.16 shows the absorption spectra of LiF crystals irradiated at the TVLPS with a) yttrium and b) copper target. The figures report the calculated x-ray fluence for single shot exposure according to formula 3.1. The x-ray fluence for the yttrium and copper targets is not comparable since it is measured in different spectral intervals (see subsection 3.2.2).

Since the bremsstrahlung contains the major part of the energy with respect to the characteristic lines, we expect a similar colouration for yttrium and copper targets. Though a high conversion efficiency into the WW region was found for yttrium [118], recent results obtained at the TVLPS indicate a high conversion efficiency for copper as well [116]. For the yttrium target the O.D. obtained for various

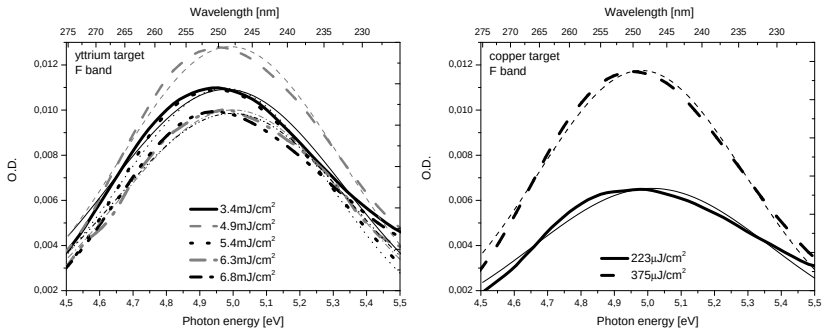

(a) (b)

Figure 4.18: Gaussian interpolation of the F band for LiF crystals irradiated at the TVLPS with a) yttrium and b) copper target. The data are represented by thick lines, the interpolations by thin lines.

single shots of the laser-plasma source does not increase with increasing x-ray fluence in the WW, but varies only slighty. Variations of the laser pulse energy induce not only variations in the x-ray energy, but also a shift in the spectrum of the bremsstrahlung, which in turn corresponds to different absorption coefficients in LiF. For the copper target, on the other hand, the O.D. follows the increase in the x-ray fluence measured with the aluminium filter. A possible explanation could be that a large part of the x-ray energy detected with the vanadium filter originates from photons in the WW spectral interval, while the colouration is due to photons of higher energy. The spectral interval of these photons might be between about 1 and 1.5 keV as measured with the aluminium filter. Since photons from 3 keV upwards are detected with the vanadium filter as well, we can exclude significant contributions from this part of the spectrum. This explanation is supported by the fact that the maximum of the bremsstrahlung

X-ray fluence $[mJ/cm^2]$	A [a.u.]	w [eV]	x_c [eV]	$\bar{R}^2$ [ ]
3.4	0.0097 ±1.02E-4	0.831 ±1.15E-2	4.97 ±3.62E-3	0.97184
4.9	0.01072 ±9.11E-5	0.787 ±8.68E-3	4.992 ±2.86E-3	0.98293
5.4	0.00871 ±6.35E-5	0.746 ±7.00E-3	4.975 ±2.39E-3	0.98824
6.3	0.00852 ±5.92E-5	0.800 ±7.23E-3	5.00 ±2.35E-3	0.98833
6.8	0.0087 ±1.00E-4	0.83 ±1.25E-2	4.997 ±3.96E-3	0.96699
0.22	0.00582 ±7.40E-5	0.84 ±1.39E-2	5.012 ±4.38E-3	0.96130
0.38	0.00918 ±6.78E-5	0.734 ±6.95E-3	4.981 ±2.40E-3	0.98814

Table 4.6: Parameters of the Gaussian interpolation of the RT F absorption band in LiF crystals irradiated at the TVLPS.

is at 700 eV, and the fluorine K edge at 696.7 eV (subsection 3.2.2). The higher colouration efficiency of photons with energies from 1 keV upwards is due to their higher energy. These theoretical considerations are supported by simulations of the deposited energy density in LiF for the bremsstrahlung spectrum of the TVLPS performed by Dr. E. Nichelatti. Fig. 4.17 shows the deposited energy density as function of distance from the surface with an attenuation length of 0.89 μm corresponding to photon energies of about 370 or 1000eV.

Fig. 4.18 shows the F band with Gaussian interpolation performed in the spectral interval between 4.5 and 5.5 eV. The data are represented by thick lines, the interpolation by thin lines. A deconvolution of the M absorption band was not attempted since it is close to the limit of instrumental sensitivity. Table 4.6 provides the parameters of the F band interpolation as well as gof. The gof is acceptable and the centre position x_c is in excellent agreement with the literature, while the FWHM deviates by up to 10%.

From the Gaussian interpolation of the M band it is possible to calculate the F-to-M ratio, which is similar for yttrium and copper targets. Its average value amounts to 23 with a standard deviation of 7. The F-to-M ratio for irradiation with a laser-plasma source is obviously smaller than for irradiation with a synchroton source. This result is comparable with the F-to-M ratio of 33 obtained for SHI and explained by the lower penetration length of soft x-rays from the laser plasma source (see subsection 4.2.1). Colouration mainly by bremsstrahlung explains the similar values for yttrium and copper targets.

4.3.2 Detector Response in PL

On the LiF crystals irradiated at the TVLPS with yttrium target and fluences of 3.4, 4.9, 5.4, 6.3 and 6.8 mJ/cm^2 as well as copper target and fluences of 223 and 375 µJ/cm^2 PL measurements in lock-in technique (subsection 3.3.2) were performed. The PL spectra were corrected for the instrumental response. The spectra with the typical emission bands of F_2 and F_3^+ centres and their devonvolution are shown in fig. 4.19 and 4.20. The parameters of the F_2 and F_3^+ emission band interpolation are summarized in tables 4.7 and 4.8, repectively, together with gof. Gof and concordance with values reported in the literatre (table 4.5) are excellent, the only deviation regards the FWHM of the F_3^+ centre emission which deviates by up to 13% from the closest

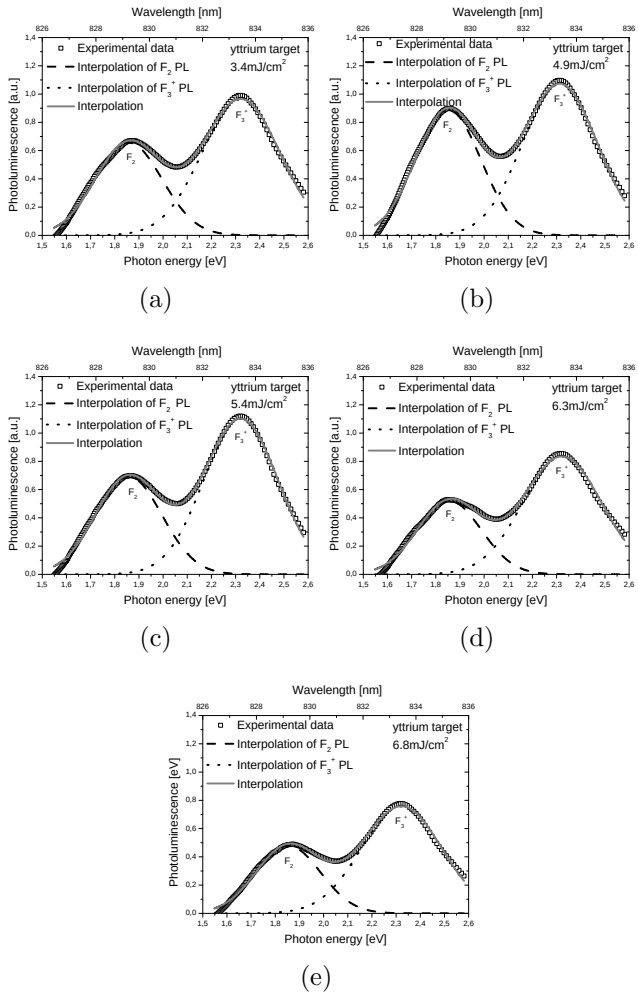

Figure 4.19: RT PL spectra of LiF crystals x-ray irradiated at the TVLPS with yttrium target and x-ray fluences of 3.4 a), 4.9 b), 5.4 c), 6.3 d) and 6.8 mJ/cm^2 e) with interpolation by two superimposed Gaussians.

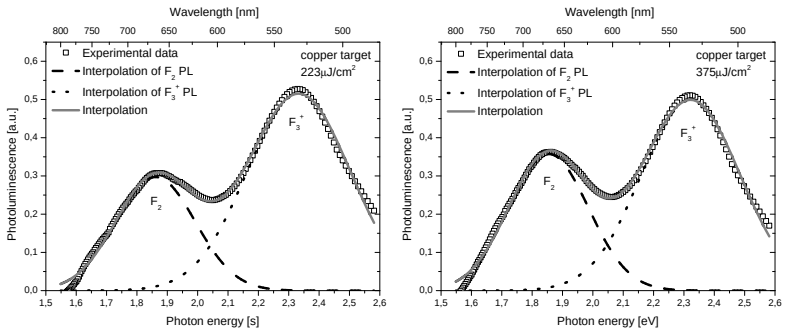

(a) (b)

Figure 4.20: Deconvolution of RT PL spectra by interpolation with two superimposed Gaussians for the LiF crystals irradiated at the TVLPS with copper target and x-ray fluences of a) 223 and b) 375 $\mu J/cm^2$.

reported value.

The F_2^+ centre emission follows the same trend as the absorption of the F band (fig. 4.21). This behaviour should be a dependence on the x-ray fluence in the spectral interval largely responsable for colouration (subsection 4.3.1). It is of interest that while deconvolution of the M absorption band is impossible, a detector in PL is able to distinguish small differences in centre density.

4.3.3 Spatial Resolution, Optical Response and Contrast

Series of LiF thin films were irradiated at the TVLPS (subsection 3.2.2) in order to analyse spatial resolution and response of LiF film based x-ray imaging detectors. Each exposure in single shot with

X-ray fluence [mJ/cm^2]	FWHM$_1$ [eV]	x_{c1} [eV]	$\bar{R}^2$ [ ]
3.39	0.325±3.55E-3	1.858±1.65E-3	0.99252
4.92	0.317±2.66E-3	1.851±1.19E-3	0.99318
5.43	0.325±2.78E-3	1.857±1.24E-3	0.99568
6.31	0.312±4.00E-3	1.856±1.86E-3	0.99121
6.81	0.315±3.49E-3	1.854±1.64E-3	0.99336
0.223	0.309±3.85E-3	1.861±1.83E-3	0.99325
0.375	0.309±3.24E-3	1.854±1.49E-3	0.99294

Table 4.7: Parameters of the Gaussian interpolation of the RT F_2 emission band in LiF crystals irradiated at the TVLPS with yttrium and copper targets.

yttrium target was performed on 100 nm thin films on glass and silicon substrates, 1 μm films on glass and silicon substrates. A LiF crystal was included in each series as reference and for spectrophotometer and spectrofluorometer measurements. Contact x-ray microradiographies of a nickel mesh (2000 lines/inch, 4 μm thick) and of a dragonfly wing on LiF film detectors with different thicknesses and substrates (see table 3.1 were produced and analysed.

The microradiographies on LiF films were read by the CLSM in fluorescence mode. We acquired series of CLSM images with a pixel dwell of 3.84 μs using the 40x objective with NA 0.6. Measurements were performed with a pinhole aperture of 100 μm and averaged over five scans. The red channel of the CLSM detects F_2 centre PL, while the green channel detects F_3^+ centre PL. Areas of

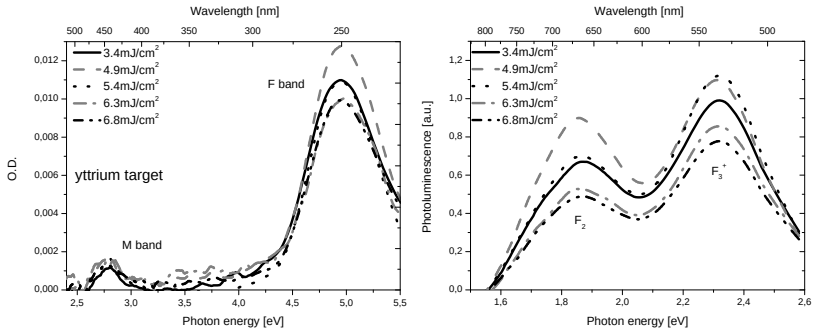

(a) (b)

Figure 4.21: RT absorption a) and emission b) spectra for five LiF crystals irradiated at the TVLPS with yttrium target.

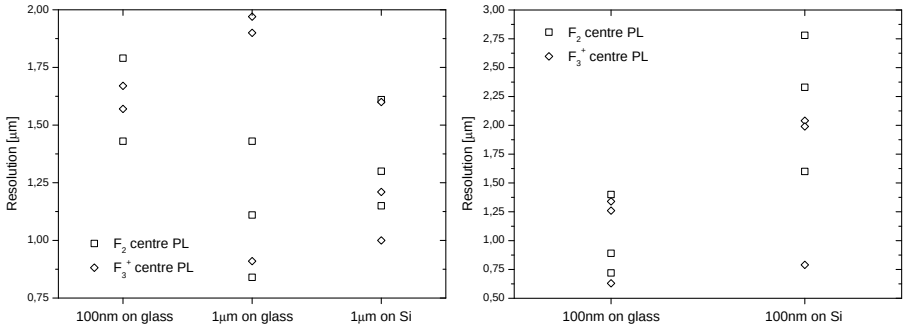

(a) (b)

Figure 4.22: Resolution of LiF samples irradiated at the TVLPS covered with copper mesh a) and parts of a dragonfly wing b).

X-ray fluence [mJ/cm^2]	FWHM$_2$ [eV]	x_{c2} [eV]
3.39	0.381±3.80E-3	2.322±1.25E-3
4.92	0.367±3.33E-3	2.314±1.13E-3
5.43	0.362±2.57E-3	2.3218±8.70E-4
6.31	0.386±4.17E-3	2.323±1.34E-3
6.81	0.394±3.77E-3	2.323±1.19E-3
0.223	0.400±4.06E-3	2.333±1.23E-3
0.375	0.385±3.89E-3	2.322±1.25E-3

Table 4.8: Parameters of the Gaussian interpolation of the RT F_3^+ emission band in LiF crystals irradiated at the TVLPS with yttrium and copper targets.

(28.6x28.6) and (25.1x25.1) μm for F_2 and F_3^+ PL, respectively, were scanned with pixel dimensions of (179x179) and (157.1x157.1)nm, with (160x160)pixel images each. For resolution measurements, the gain of the photomultipliers was optimized in each acquisition to have a better signal-to-noise ratio, while for analysis of the contrast the gain was kept constant at 6 and 5 for the green and red channel, respectively.

Fig. 4.22 shows the spatial resolution values (calculated as described in subsection 3.3.5) obtained for the contact microradiographies of the copper mesh a) and of the dragonfly wing b) on different LiF film detectors read by a CLSM. In this series of measurements we obtained a minimum spatial resolution of 630 nm. The intrinsic resolution of the LiF detector is connected to the CC dimension in the atomic scale and its migration of a few lattice distances [2], while the

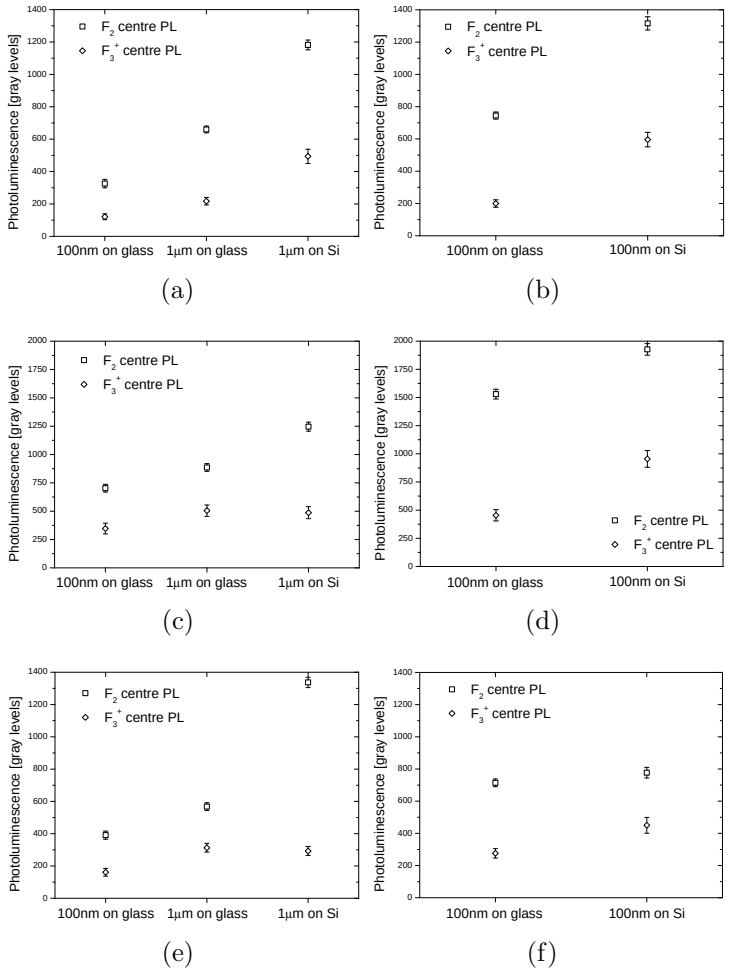

Figure 4.23: CLSM reponse of the three mixed series of LiF thin films irradiated at the TVLPS, a), c) and e) of LiF detectors covered with copper mesh, b), d) and f) of LiF detectors covered with parts of a dragonfly wing.

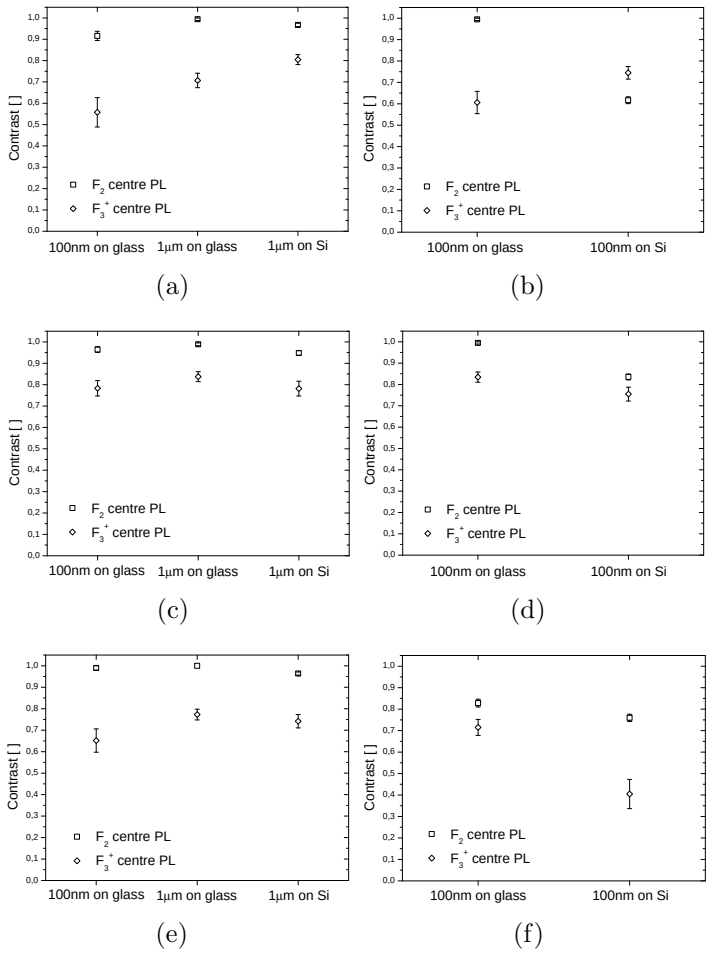

Figure 4.24: Contrast of the three mixed series of LiF thin films irradiated at the TVLPS, a), c) and e) of LiF detectors covered with copper mesh, b), d) and f) of LiF detectors covered with parts of a dragonfly wing. The microradiographies on LiF film based detectors were read by the CLSM system.

resolution of the CLSM with 40x objective and an NA of 0.6 amounts to 361 nm for F_3^+ centre emission. There is no trend in the resolution as function of thin film growth parameters such as thickness or substrate, though there is a large variation in the obtained resolutions. Resolution in x-ray contact microscopy is limited by two mechanisms: diffraction blurring $\sqrt{\lambda G}$ and penumbra blurring $G\phi/d$. Here λ is the wavelength, G the sample-detector distance, ϕ the diameter of the x-ray source and d the source-sample distance. In our experimental conditions (G≈100μm, λ=1.65nm, ϕ=400μm, d=4cm) we obtained a diffraction blurring of 0.4 μm and a penumbra blurring of 1 μm. Of course contributions from larger wavelengths have to be considered as well, but since it is possible to achieve resolutions close to the resolution of the CLSM these should not play an essential role. Thus resolution does not depend as much on detector properties or irradiation parameters as on the contact between sample and detector. To improve the contact work is in progess on a sample holder for both dry and in vivo samples.

The response detected by CLSM signal measurements of the three series of LiF thin films is plotted in fig. 4.23. For all thin films covered with parts of the dragonfly wing there is a larger response for both F_2 and F_3^+ centres from the films on Si substrate. This trend is reproduced in F_2 centre PL for the films covered by the nickel mesh. These results confirm that mechanisms related to the higher reflectivity of the Si substrate (see subsection 4.3.2) indeed increase the PL signal. Dependence on parameters of the laser excitation such as angle of incidence and excitation volume have to be carefully investigated before one can think to optimize and utilize these phenomena. Fig. 4.24 shows the contrast of the same microradiographies on LiF film detectors read by CLSM. Fig. 4.24 a) demonstrates that the increased reflectivity does not diminish the contrast; on the contrary, there is an excellent contrast with values close to 1 especially for F_2 centre PL. The lower contrast of the microradiographies on silicon substrate

in fig. 4.24 b) is due to the biological sample with its variations in thickness and composition. The contrast in F_3^+ centre PL is slightly diminished due to a lower signal-to-noise ratio.

4.3.4 X-ray Imaging of a Biological Sample

A soft x-ray microradiography of a crane fly wing on a LiF detector is presented as an example for semiquantitative analysis. The wing was put in contact with a 1 μm thick LiF film with a diameter of 18 mm on a glass substrate and irradiated with several shots of the laser plasma source to increase colouration and thus the signal-to-noise ratio during read-out process. In this experiment the sample was irradiated with seventeen shots resulting in a total x-ray fluence of 3.72 mJ/cm^2, measured with the 25 μm thick aluminium filter in front of the PIN diode. The x-ray microradiography stored in the LiF film was read out with the CLSM in fluorescence mode with the 4x objective, a pinhole diameter of 150 μm and a pixel dwell of 1.44 μs. The F_2 centre fluorescence image acquired with a gain of 5 shows a (1.74x1.74) mm area with a pixel size of (0.9x0.9) μm.

Fig. 4.25 shows the fluorescence image of the crane fly wing and the intensity profiles along the white lines. The average diameter of the rib (profile b)) was determined to 13 μm. Profile c) shows the intensity difference between the uncovered detector and the part covered by the crane fly wing. Profile a), on the other hand, shows the difference between the part of the detector covered by one layer of the crane fly wing and another part where two or more layers are superimposed. The thickness of the crane fly wing may be determined from the thickness of the rib and controlled by comparison with the thickness of two layers.

Due to the absorption of the rib the local fluorescence intensity decreases from E_{r0}=1574 to E_r=461 gray levels, while absorption of one layer of the wing decreases the intensity from E_{i0}=2322 to E_i=1394

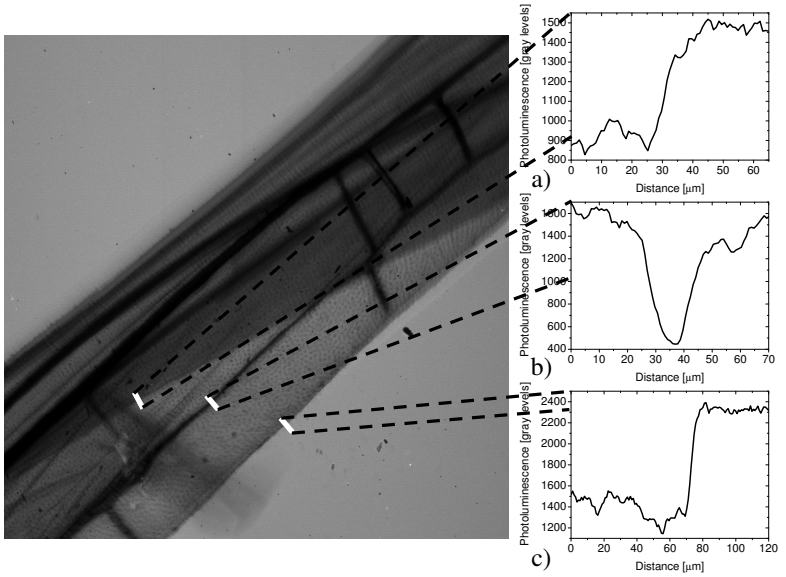

Figure 4.25: (1.74x1.74) mm fluorescence image of the soft x-ray microradiography of a crane fly wing on a 1 μm LiF thin film on glass substrate with several intensity profiles a), b) and c) along the white lines.

gray levels. With these values the thickness of the crane fly wing calculated with formula 3.20 amounts to 5.4 μm. Confronting the absorption of one layer with 5.4 μm thickness with the absorption of two or more layers (the fluorescence intensity decreases from E_{i0}=2322 to E_i=919 gray levels) we obtain a thickness of 9.8 μm for the latter. This means that there are two superimposed layers and that with E_{r0}=1574 and E_r=461 we can calculate the thickness of one layer from the difference in fluorescence intensity between one and two layers as well (the fluorescence intensity decreases from E_{i0}=1481 to E_i=919 gray levels). With these values we obtain a thickness of 5.1 μm for one layer which gives a thickness of 9.9 μm for two layers. These results are in excellent concordance.

Chapter 5

Conclusions

In the present thesis I performed the optical characterization of LiF-based detectors for imaging applications with polychromatic hard and soft x-rays. This work demonstrates that LiF x-ray imaging detectors, based on the optical reading of the PL of stable electronic point defects, combine high spatial resolution of a few hundred nanometer with simplicity of use and a large dynamic range.

The formation of stable electronic defects was obtained both for irradiation with hard x-rays (at several irradiation times) and for single-shot irradiation with soft x-rays. In x-ray irradiated LiF crystals absorption spectra were measured and analysed and the PL signal was found proportional to the absorption band intensity. The PL measurement allows to distinguish differences in the concentration of aggregated defects and to investigate the optical response as function of irradiation time and growth parameters in x-ray irradiated LiF crystals and thin films.

For the first time LiF crystals and thin films irradiated at x-ray energies between 6 and 40 keV were investigated. LiF crystal detectors show a linear PL response over two decades for both kinds of aggregated defects in the investigated irradiation conditions. A linear PL

response was also obtained for LiF films only 1 μm thick. In the analysed experimental conditions the colouration kinetics of LiF crystals and films are the same. The sensitivity of the PL reading technique is suitable for x-ray imaging experiments at very short irradiation times (1 s) even on LiF thin films.

The z-scan technique of the CLSM was employed to determine the colouration depth of x-rays in LiF and to study the effects of the sample optical characteristics on these measurements.

A spatial resolution down to 630 nm was obtained for single shot soft x-ray contact imaging experiments. Spatial resolution is largely independent of detector characteristics. It depends mainly on the contact between sample and detector and can be optimized by development of a suitable sample holder. In agreement with modelling [149, 150] LiF thin films on silicon substrate exhibit a larger PL response than films on glass substrate, mainly due to the reflectivity of the substrate at the optical wavelengths. The high dynamic range of x-ray imaging LiF film detectors was exploited to estimate the thickness of a crane fly wing from its microradiography.

This thesis was realized with the scientific-technological and didactic support of the ENEA.

Bibliography

[1] J. Kirz, C. Jacobsen, and M. Howells. *Q. Rev. Biophys.*, 28:33, 1995.

[2] G. Baldaccini, S. Bollanti, F. Bonfigli, F. Flora, P. Di Lazzaro, A. Lai, T. Marolo, R.M. Montereali, D. Murra, A. Faenov, T. Pikuz, E. Nichelatti, G. Tomassetti, A. Reale, L. Reale, A. Ritucci, T. Limongi, L. Palladino, M. Francucci, S. Martellucci, and G. Petrocelli. *Rev. Sci. Instrum.*, 76:113104, 2005.

[3] S. Almaviva, F. Bonfigli, I. Franzini, A. Lai, R. M. Montereali, D. Pelliccia, A. Cedola, and S. Lagomarsino. *Appl. Phys. Lett.*, 89:054102, 2006.

[4] G. Baldacchini, M. Cremona, G. d'Auria, R.M. Montereali, and V. Kalinov. *Phys. Rev. B*, 54:17508, 1996.

[5] F. Bonfigli, A. Faenov, F. Flora, M. Francucci, P. Gaudio, A. Lai, S. Martellucci, R.M. Montereali, T. Pikuz, L. Reale, M. Richetta, M.A. Vincenti, and G. Baldacchini. *Microsc. Res. Tech.*, 71:35, 2008.

[6] `http://henke.lbl.gov/optical_constants/`.

[7] R.M. Montereali, G. Baldacchini, F. Bonfigli, M.A. Vincenti, and S. Almaviva. Il microscopio confocale a scansione laser: uno

strumento versatile per la caratterizzazione di microdispositivi e nanostrutture. Technical Report RT/2008/40/FIM, ENEA, 2008.

[8] H.S. Nalwa. *Handbook of Thin Film Materials*, chapter 7. Academic Press, 2002.

[9] J. Nahum and D.A. Wiegand. *Phys. Rev.*, 154:817, 1967.

[10] V.V. Ter-Mikirtychev and T.T. Tsuboi. *Prog. Quantum Electr.*, 20:219, 1996.

[11] A. Ustione, A. Cricenti, F. Bonfigli, F. Flora, A. Lai, T. Marolo, R. M. Montereali, G. Baldacchini, A. Faenov, T. Pikuz, and L. Reale. *Appl. Phys. Lett.*, 88:141107–9, 2006.

[12] F. Bonfigli, F. Flora, I. Franzini, E. Nichelatti, and R.M. Montereali. *J. Lum.*, 129:1964, 2009.

[13] F. Bonfigli, S. Almaviva, I. Franzini, R.M. Montereali, A. Cedola, S. Lagomarsino, and D. Pelliccia. *Radiat. Meas.*, 45:599, 2010.

[14] R.M. Montereali, S. Almaviva, F. Bonfigli, A. Faenov, F. Flora, I. Franzini, E. Nichelatti, T. Pikuz, M.A. Vincenti, and G. Baldacchini. *Proc. SPIE*, 6593:65932B, 2007.

[15] F. Ranwez. *Comptes Rendue des Séances de l'Academie des Sciences*, 122:841, 1896.

[16] W.C. Röntgen. *Sitzungsberichte der Würzburger Physik-medic. Gesellschaft*, 137:41, 1895.

[17] P. Goby. *Comptes Rendue des Séances de l'Academie des Sciences*, 156:686, 1913.

[18] V.E. Cosslett and W.C. Nixon. *X-ray Microscopy*. Cambridge University Press, 1960.

[19] Y. Wang and C. Jacobsen. *J. Microsc.*, 191:159, 1998.

[20] E. Spiller, R. Feder, J. Topalian, D. Eastman, W. Gudat, and D. Sayre. *Science*, 191:1172, 1976.

[21] R. Feder, D. Sayre, E. Spiller, J. Topalian, and J. Kirz. *J. Appl. Phys.*, 47:1192, 1976.

[22] B. Niemann, D. Rudolph, and G. Schmahl. *Appl. Opt.*, 15:1883, 1976.

[23] D. Sayre, J. Kirz, R. Feder, D. M. Kim, and E. Spiller. *Science*, 196:1339, 1977.

[24] A.M. Kondratenko and A.N. Skrinsky. *Opt. Spectrosc.*, 42:189, 1977.

[25] P. Albertano, L. Reale, L. Palladino, A. Reale, R. Cotton, S. Bollanti, P. Di Lazzaro, F. Flora, N. Lisi, A. Nottola, K. Vigli Papadaki, T. Letardi, D. Banai, A. Conti, M. Moret, and A. Grilli. *J. Microsc.*, 187:96, 1997.

[26] B.J. Panessa, R. McCorkle, P. Hoffman, J.B. Warren, and G. Coleman. *Ultramicrosc.*, 6:139, 1981.

[27] B. Kaulich, P. Thibault, A. Gianoncelli, and M. Kiskinova. *J. Phys.: Condens. Matter*, 23:083002, 2011.

[28] G. Poletti, F. Orsini1, D. Batani, A. Bernardinello, T. Desai, J. Ullschmied, J. Skala, B. Kralikova, E. Krousky, L. Juha, M. Pfeifer, Ch. Kadlec, T. Mocek, A. Präg, O. Renner, F. Cotelli, C. Lora Lamia, and A. Zullini. *Eur. Phys. J. D*, 30:235, 2004.

[29] A.C. Cefalas, P. Argitis, Z. Kollia, E. Sarantopoulou, T.W. Ford, A.D. Stead, A. Marranca, C.N. Danson, J. Knott, and D. Neely. *Appl. Phys. Lett.*, 72:3258, 1998.

[30] G. Poletti, F. Orsini, and D. Batani. *Solid State Phenom.*, 107:7, 2005.

[31] D. Batani, C. Botto, M. Moret, M. Milani, G. Lucchini, K. Eidmann, F. Cotelli, C. Lora Lamia Donin, G. Poletti, T. Ford, and A. Stead. *Eur. Phys. J. D*, 21:167, 2002.

[32] M. Kado, M. Ishino, S. Tamotsu, K. Yasuda, M. Kishimoto, M. Nishikino, Y. Kinjo, , and K. Shinohara. *AIP Conf. Prog.*, 1365:391, 2011.

[33] A.N. Danilewsky, A. Rack, J. Wittge, T. Weitkamp, R. Simon, H. Riesemeier, and T. Baumbach. *Nucl. Instrum. Methods Phys. Res. B*, 266:2035, 2008.

[34] J. Jakubek. Semiconductor pixel detectors and their applications in life sciences. Technical report, Czech Technical University in Prague, 2009.

[35] F. Bonfigli, R.M. Montereali, and G. Baldacchini. Photoluminescent lithium fluoride films as innovative x-ray imaging detectors.

[36] R.M. Montereali, G. Baldacchini, and L.C. Scavarda Do Carmo. *Thin Solid Films*, 205:106, 1991.

[37] G. Baldacchini, F. Menchini, and R.M. Montereali. *Il nuovo Cim.*, 20 D:845, 1998.

[38] M. Kumar, F. Singh, S.A. Khan, V. Baranwal, S. Kumar, D.C. Agarwal, A.M. Siddiqui, A. Tripathi, A. Gupta, D.K. Avasthi, and A.C. Pandey. *J. Phys. D: Appl. Phys.*, 38:637, 2005.

[39] A.M.E. Santo, L.C. Courrol, I.M. Ranieri, N.U. Wetter, N.D. Vieira Jr., and S.L. Baldochi. *Opt. Mat.*, 27:487, 2004.

[40] G. Baldacchini, F. Bonfigli, F. Menchini, and R.M. Montereali. *Nucl. Instrum. Meth. Phys. Res. B*, 191:216, 2002.

[41] H. Gu and H. Liu. *Opt. Commun.*, 201:113, 2002.

[42] K. Kawamura, M. Hirano, T. Kamiya, and H. Hosono. *J. Non-Cryst. Solids*, 352:2347, 2006.

[43] R.M. Montereali, F. Bonfigli, L. Gregoratti abd M. Kiskinova, R. Larciprete, M. Montecchi, and E. Nichelatti. *J. Non-Cryst. Solids*, 353:456, 2007.

[44] I. Franzini. Realizzazione, caratterizzazione e miglioramento di un rivelatore di immagini ai raggi-x su fluoruro di litio. Master's thesis, Ingegneria Elettronica, 2006.

[45] K. Schwartz, C. Trautmann, A.S. El-Said, R. Neumann, M. Toulemonde, and W. Knolle. *Phys. Rev. B*, 70:184104, 2004.

[46] J. Maniks, I. Manika, R. Grants, R. Zabels, K. Schwartz, M. Sorokin, and R.M. Papaleo. *Appl. Phys. A*, 104:1121, 2011.

[47] G. Baldacchini, S. Bollanti, F. Bonfigli, P. Di Lazzaro, A.Y. Faenov, F. Flora, T. Marolo, R.M. Montereali, D. Murra, E. Nichelatti, T. Pikuz, A. Reale, L. Reale, A. Ritucci, and G. Tomassetti. *IEEE J. Sel. Top. Quant. Electron.*, 10:1435, 2004.

[48] E.D. Palik. *Handbook of Optical Constants of Solids*. Academic Press, 1985.

[49] D.G. Lord and T.E. Gallon. *Surf. Sci.*, 36:606, 1973.

[50] V. Mussi, F. Granone, C. Boragno, F. Buatier de Mongeot, U. Valbusa, T. Marolo, and R.M. Montereali. *Appl. Phys. Lett.*, 88:103116, 2006.

[51] R.M. Montereali, G. Baldacchini, S. Martelli, and L.C. Scavarda do Carmo. *Thin Solid Films*, 196:75, 1991.

[52] G. Baldacchini, M. Cremona, G. d'Auria, S. Martelli, R.M. Montereali, M. Montecchi, E. Burattini, A. Grilli, and A. Raco. *Nucl. Instrum. Meth. Phys. Res. B*, 116:447, 1996.

[53] P.E. Di Nunzio, L. Fornarini, S. Martelli, and R.M. Montereali. *Phys. Stat. Sol. A*, 164:747, 1997.

[54] H.K. Pulker. *Appl. Opt.*, 18:1969, 1979.

[55] G. Baldacchini, E. Burattini, L. Fornarini, A. Mancini, S. Martelli, and R.M. Montereali. *Thin Solid Films*, 330:67, 1998.

[56] K. Schwartz, C. Trautmann, and R. Neumann. *Nucl. Instrum. Meth. Phys. Res. B*, 209:73, 2003.

[57] T.J. Pearsal. *J. Roy. Inst.*, 1:77, 1830.

[58] R. Hilsch and R.W. Pohl. *Z. Phys.*, 48:384, 1928.

[59] J. Frenkel. *Phys. Rev.*, 37:17, 1931.

[60] R.S. Knox. *Solid State Physics*, chapter Theory of Excitons. Academic Press, 1963.

[61] T.G. Castner and W. Känzig. *J. Phys. Chem. Solids*, 3:178, 1957.

[62] H. Hersh. *Phys. Rev.*, 148:928, 1966.

[63] Ch. Lushchik, I.K. Vitol, and M.A. Elango. *Sov. Phys. Usp.*, 20:489, 1977.

[64] D. Pooley. *Proc. Phys. Soc.*, 87:245, 1966.

[65] F. Agullo-Lopez, C.R.A. Catlow, and P.D. Townsend. *Point defects in materials*. Academic Press, 1988.

[66] K. Schwartz, A.E. Volkov, M.V. Sorokin, C. Trautmann, K.-O. Voss, R. Neumann, and M. Lang. *Phys. Rev. B*, 78:924120, 2008.

[67] A.C. Lushchik and C.B. Lushchik. *Phys. Ser.*, 56:201, 1992.

[68] W. Meise, U. Rogulis, F.K. Koschnik, K.S. Song, and J.M. Spaeth. *J. Phys.: Condens. Matter*, 6:1815, 1994.

[69] G. Baldacchini, G. d'Auria, R.M. Montereali, and A. Scacco. *J. Phys.: Condens. Matter*, 10:857, 1998.

[70] N. Itoh and A.M. Stoneham. *Materials Modification by Electronic Excitation*. Cambridge University Press, 2001.

[71] N. Itoh and K. Tanimura. *Radiat. Eff.*, 98:435, 1986.

[72] Y. Farge. *J. Phys. Chem. Solids*, 30:1375, 1969.

[73] J.L. Alvarez-Rivas and P.W. Levy. *Phys. Rev.*, 162:816, 1967.

[74] F. Agullo-Lopez and F. Jaque. *J. Phys. Chem. Solids*, 34:1949, 1973.

[75] M. Aguilar, F. Agullo-Lopez, and F. Jaque. *Radiat. Eff.*, 61:215, 1982.

[76] P. Thévenard, G. Guiraud, C.H.S. Dupuy, and B. Delaunay. *Radiat. Eff.*, 32:83, 1977.

[77] J.V.R. Kaufman and C.D. Clark. *J. Chem. Phys.*, 38:1388, 1963.

[78] G. Baldacchini, M. Cremona, U.M. Grassano, V. Kalinov, and R.M. Montereali. Emission properties of gamma irradiated lif crystals excited in the f absorption band by an excimer laser. In *Defects in Insulating Materials*, 1993.

[79] T.T. Basiev, S.B. Mirov, and V.V. Osiko. *IEEE J. Quantum Electron.*, 24:1052, 1988.

[80] M. Montecchi, E. Nichelatti, A. Mancini, and R.M. Montereali. *J. Appl. Phys.*, 86:3745, 1999.

[81] G. Baldacchini, E. De Nicola, R.M. Montereali, A. Scacco, and V. Kalinov. *J. Phys. Chem. Solids*, 64:21, 2000.

[82] A. Perez, J. Davenas, and C.H.S. Dupuy. *Nucl. Instrum. Methods*, 132:219, 1976.

[83] V.V. Valeri, T. Mikirtychev, and T. Tsuboi. *Canad. J. Phys.*, 75:813, 1997.

[84] F. Bonfigli, S. Almaviva, G. Baldacchini, S. Bollanti, F. Flora, A. Lai, R.M. Montereali, E. Nichelatti, G. Tomassetti, A. Ritucci, L. Reale, A.Y. Faenov, T.A. Pikuz, R. Larciprete, L. Gregoratti, and M. Kiskinova. *Spectrochim. Act. Part B*, 62:631, 2007.

[85] A. Lushchik, Ch. Lushchik, K. Schwartz, E. Vasilchenko, R. Papaleo, M. Sorokin, A.E. Volkov, R. Neumann, and C. Trautmann. *Phys. Rev. B*, 76:054114, 2007.

[86] G. Cheng, Y. Wang, J. He, G. Chen, and W. Zhao. *Opt. Express*, 15:8938, 2007.

[87] P.M. Adam, S. Benrezzak, J.L. Bijeon, P. Royer, S. Guy, B. Jacquier, P. Moretti, R.M. Montereali, M. Piccinini, F. Menchini, F. Somma, C. Seassal, and H. Rigneault. *Opt. Express*, 9:353, 2001.

[88] T.T. Basiev, S.B. Mirov, and V.V. Osiko. *IEEE J. Quantum Electron.*, 24:1052, 1988.

[89] S.V. Godbole and A.G. Page. *Pramana*, 42:79, 1994.

[90] G. Baldacchini, F. De Matteis, R. Francini, U.M. Grassano, F. Menchini, and R.M. Montereali. *J. Lum.*, 87-89:580, 2000.

[91] G. Baldacchini, S. Bigotta, and R.M. Montereali. *J. Lum.*, 94-95:299, 2001.

[92] G. Baldacchini, E. De Nicola, G. Giubileo, F. Menchini, G. Messina, R.M. Montereali, and A. Scacco. *Nucl. Instrum. Meth. Phys. Res. B*, 141:542, 1998.

[93] R.M. Montereali, T. Marolo, M. Montecchi, and E. Nichelatti. *Nucl. Instrum. Meth. Phys. Res. B*, 268:2866, 2010.

[94] S. Paciornik, R.A. Nunes, J.P. von der Weid, L.C. Scavarda do Carmo, and V.S. Kalinov. *J. Phys. D: Appl. Phys.*, 24:1811, 1991.

[95] G. Baldacchini, R.M. Montereali, E. Nichelatti, V.S. Kalinov, A.P. Voitovich, A.T. Davidson, and A.G. Kozakiewicz. *J. Appl. Phys.*, 104:063712, 2008.

[96] W.L. McLaughlin, A. Miller, S.C. Ellis, A.C. Lucas, and B.M. Kapsar. *Nucl. Instrum. Methods Phys. Res. B*, 175:17, 1980.

[97] U. Kaiser, N. Kaiser, P. Weissbrodt, U. Mademann, E. Hacker, and H. Mueller. *Thin Solid Films*, 217:7, 1992.

[98] R.M. Montereali, A. Mancini, S. Martelli, F. Menchini, and P. Picozzi. *Appl. Organometal. Chem.*, 15:407, 2001.

[99] G. Baldacchini and R.M. Montereali. *Opt. Mat.*, 16:53, 2001.

[100] F. Barkusky, C. Peth, K. Mann, T. Feigl, and N. Kaiser. *Rev. Sci. Instrum.*, 76:105102, 2005.

[101] F. Bonfigli, M.A. Vincenti, S. Almaviva, R.M. Montereali, E. Nichelatti, R.N. Nogueira, and H.J. Kalinowski. *Appl. Opt.*, 48:G38, 2009.

[102] G. Tomassetti, A. Ritucci, A. Reale, L. Arrizza, F. Flora, R.M. Montereali, A. Faenov, and T. Pikuz. *Appl. Phys. Lett.*, 85:4163, 2004.

[103] R.M. Montereali, A. Mancini, G.C. Righini, and S. Pelli. *Opt. Commun.*, 153:223, 1993.

[104] R.M. Montereali, M. Piccinini, and E. Burattini. *Appl. Phys. Lett.*, 78:4082, 2001.

[105] J.A.M. Pereira, M. Cremona, S. Pelli, E.L.A. Macchione, K. Koide, S.S. Vasconcelos, and G.C. Righini. *Nucl. Instrum. Meth. Phys. Res. B*, 240:234, 2005.

[106] A. Belarouci, F. Menchini, H. Rigneault, B. Jacquier, R.M. Montereali, F. Somma, and P. Moretti. *Opt. Commun.*, 189:281, 2001.

[107] F. Bonfigli, B. Jacquier, F. Menchini, R.M. Montereali, P. Moretti, E. Nichelatti, M. Piccinini, H. Rigneault, and F. Somma. *Radiat. Eff. Def. Solids*, 158:185, 2003.

[108] F. Bonfigli, M. Cathelinaud, B. Jacquier, R.M. Montereali, P. Moretti, E. Nichelatti, M. Piccinini, H. Rigneault, and F. Somma. *Opt. Commun.*, 233:389, 2004.

[109] K. Kawamura, D. Takamizu, T. Kurobori, T. Kamiya, M. Hirano, and H. Hosono. *Nucl. Instrum. Meth. Phys. Res. B*, 218:332, 2004.

[110] H. Gu, K. Wang, and H. Liu. *Chin. Phys. Lett.*, 18:1604, 2001.

[111] William Conway, B. Rami Reddy, and R.R. Kalluru. *J. Lum.*, 107:249, 2004.

[112] V.V. Federov, S.B. Mirov, M. Ashenafi, and L. Xie. *Appl. Phys. Lett.*, 79:2318, 2001.

[113] W.E. Moerner, P. Pokrowsky, F.M. Schellenberg, and G.C. Bjorklund. *Phys. Rev. B*, 33:5702, 1986.

[114] A. Rack, T. Weitkamp, S. Bauer Trabelsi, P. Modregger, A. Cecilia, T. dos Santos Rolo, T. Rack, D. Haas, R. Simon, R. Heldele, M. Schulz, B. Mayzel, A.N. Danilewsky, T. Waterstradt, W. Diete, H. Riesemeier, B.R. Mller, and T. Baumbach. *Nucl. Instrum. Meth. Phys. Res. B*, 267:1978, 2009.

[115] S. Gambino, G. Baldacchini, I. Franzini, R.M. Montereali, M.A. Vincenti, and V. Mussi. Crescita e caratterizzazione di film sottili di fluoruro di litio. Technical Report RT/2006/68/FIM, ENEA, 2006.

[116] M. Francucci, P. Gaudio, S. Martellucci, and M. Richetta. *International Journal of Spectroscopy*, 2011:792131, 2011.

[117] D. Attwood. *Soft X-rays and Extreme Ultraviolet Radiation: Principles and Applications*. Cambridge University Press, 1999.

[118] H. Kondo and T. Tomie. *J. Appl. Phys.*, 75:3798, 1994.

[119] M. Francucci. *Sistemi per la generazione di raggi X da plasma indotto da laser e possibili applicazioni*. PhD thesis, Ingegneria dei Microsistemi, 2005.

[120] `http://www.kayelaby.npl.co.uk/atomic_and_nuclear_physics/4_2/4_2_1.html`.

[121] `http://xdb.lbl.gov/Section1/Table_1-2.pdf`.

[122] F. Bonfigli, M. Montecchi, R.M. Montereali, E.Nichelatti, M. Piccinini, and F. Somma. *J. Phys.: Conf. Ser.*, 249:012004, 2010.

[123] W.B. Fowler. *Physics of Color Centers*. Academic Press, 1968.

[124] J.H. Shulman and W.D. Compton. *Color Centers in Solids*. Macmillan, 1962.

[125] R. Bate and C. Heer. *J. Phys. Chem. Solids*, 7:14, 1958.

[126] D. Semwogerere and E.R. Weeks. *Encyclopedia of Biomaterials and Biomedical Engineering*, chapter Confocal Microscopy. Taylor & Francis, 2005.

[127] A. Diaspro, editor. *Confocal and two-photon microscopy: foundations, applications and advances*. Wiley-Liss, 2002.

[128] S. Grill and E.H.K. Stelzer. *J. Opt. Soc. Am.*, 16:2658, 1999.

[129] S. Wilhelm, B. Gröbler, M. Gluch, and H. Heinz. *Confocal Laser Scanning Microscopy: Principles*.

[130] E. Nichelatti, F. Bonfigli, A.Y. Faenov, F. Flora, T. Marolo, M. Montecchi, R.M. Montereali, T. Pikuz, and G. Baldacchini. *J. Non-Cryst. Solids*, 351:1774, 2005.

[131] *Origin User's Manual*.

[132] Y. Liu, J.C. Andrews, F. Meirer, A. Mehta, S. Carrasco Gil, P. Sciau, Z. Mester, and P. Pianetta. *AIP Conf. Proc.*, 1365:357, 2011.

[133] P. Pringsheirn and P. Yuster. *Phys. Rev.*, 78:293, 1950.

[134] C.C. Klick. *Phys. Rev.*, 79:894, 1950.

[135] C.J. Delbecq and P. Pringsheirn. *J. Appl. Phys.*, 21:794, 1953.

[136] R. Kalo, K. Nakashima, and Y. Uchida. *J. Phys. Soc. Japan*, 15:2111, 1960.

[137] H. Rabin and C.C. Klick. *Phys. Rev.*, 117:1005, 1960.

[138] R.T. Bate and C.V. Heer. *J. Phys. Chem. Solids*, 7:14, 1958.

[139] J.J. Gilman and W.G. Johnston. *J. Appl. Phys.*, 29:877, 1958.

[140] E. Hughes, D. Pooley, H.U. Rahman, and W.A. Runciman. Technical Report R-5604, Harwell Atomic Research Establishment, 1967.

[141] F. Bonfigli, P. Gaudio, I. Lupelli, E. Nichelatti, M. Richetta, M.A. Vincenti, and R.M. Montereali. *IOP Conf. Ser.: Mat. Sci. Eng.*, 15:012025, 2010.

[142] R.M. Montereali, S. Almaviva, F. Bonfigli, I. Franzini, D. Pelliccia, A. Cedola, and S. Lagomarsino. *J. Phys.: Conf. Ser.*, 249:012003, 2010.

[143] V.A. Skuratov, S.M. Abu AlAzm, and V.A. Altynov. *Nucl. Instrum. Meth. Phys. Res. B*, 191:251, 2002.

[144] C. Trautmann, K. Schwartz, J.M. Costantini, T. Steckenreiter, and M. Toulemonde. *Nucl. Instrum. Meth. Phys. Res. B*, 146:367, 1998.

[145] C. Trautmann, M. Toulemonde, K. Schwartz, J.M. Costantini, and A. Müller. *Nucl. Instrum. Meth. Phys. Res. B*, 164-165:365, 2000.

[146] L.C. Courrol, R.E. Samad, O.E. Martinez, L. Gomes, I.M. Ranieri, S.L. Baldochi, A.Z. de Freitas, and N.D. Vieira Junior. *J. Opt. A: Pure Appl. Opt.*, 10:104023, 2008.

[147] Y. Farge, G. Toulouse, and M. Lambert. *J. Physique*, 27:287, 1996.

[148] R.M. Montereali, S. Almaviva, F. Bonfigli, A. Cricenti, A. Faenov, F. Flora, P. Gaudio, A. Lai, S. Martellucci, E. Nichelatti, T. Pikuz, L. Reale, M. Richetta, and M.A. Vincenti. *Nucl. Instrum. Methods Phys. Res. B*, 623:758, 2010.

[149] E. Nichelatti, S. Almaviva, F. Bonfigli, I. Franzini, R.M. Montereali, and M.A. Vincenti. *Nucl. Instrum. Meth. Phys. Res. B*, 268:3035, 2010.

[150] E. Nichelatti. Cooperative spontaneous emission from volume sources in layered media. Technical Report RT/2009/4/FIM, ENEA, 2009.